Journal of Controlled Release 399 (2026) 115289

Contents lists available at ScienceDirect

Journal of Controlled Release

journal homepage: www.elsevier.com/locate/jconrel

Dual-restricted AAV gene delivery *via* suprachoroidal administration mediates precision RPE SOCS3 restoration for dry age-related macular degeneration

Yiquan Zhang [a], Fuxiao Luan [a], Jing Feng [a,**], Wenqiang Sun [b,**], Yong Tao [a,c,d,*,1]

[a] Department of Ophthalmology, Beijing Chaoyang Hospital, Capital Medical University, Beijing 100020, PR China
[b] State Key Laboratory of Biopharmaceutical Preparation and Delivery, Institute of Process Engineering Chinese Academy of Sciences, Chinese Academy of Sciences, Beijing 100190, PR China
[c] National Engineering Research Center for Ophthalmology, Beijing, PR China
[d] Engineering Research Center of Ophthalmic Equipment and Materials, Ministry of Education, Beijing, PR China

ARTICLE INFO

Keywords:
Dry age-related macular degeneration
Dual-restricted gene delivery
RPE-specific Best1 promoter
Suprachoroidal delivery
SOCS3-STAT3 axis
Inflammation
Reactive oxygen species

ABSTRACT

Dry age-related macular degeneration (dAMD) is a leading cause of irreversible vision loss, driven by chronic oxidative stress and inflammation in the retinal pigment epithelium (RPE). Disruption of key negative regulators of the JAK-STAT pathway, particularly SOCS3, contributes to this oxidative-inflammatory cascade. To address this, we developed a dual-restricted ocular gene delivery platform that combines suprachoroidal administration with an RPE-specific Best1 promoter, enabling localized, durable, and cell-restricted SOCS3 expression. Comparative analysis showed that intravitreal injection poorly transduced the RPE, whereas suprachoroidal delivery improved AAV access to the RPE/outer retinal region, and the Best1 promoter further restricted expression to RPE cells, reducing neural retinal off-target expression. *In vitro*, SOCS3 restoration suppressed STAT3 activation, inflammatory cytokine release, reactive oxygen species accumulation, mitochondrial disruption, and barrier impairment. *In vivo*, the dual-restricted system achieved long-term, ocular-localized expression for at least six months, reducing microglial/macrophage activation, inflammation, oxidative stress, and apoptosis, thereby preserving outer retinal architecture. Ocular and systemic safety assessments detected no overt toxicity under the tested conditions. Together, these findings support suprachoroidal AAV-Best1-SOCS3 delivery as a dual-restricted platform for localized modulation of oxidative-inflammatory retinal degeneration and warrant further preclinical evaluation.

1. Introduction

Age-related macular degeneration (AMD) remains a leading cause of irreversible blindness among the elderly population worldwide, imposing a substantial clinical and socioeconomic burden [1]. While anti-vascular endothelial growth factor therapies have transformed the management of neovascular AMD, treatment options for dry AMD (dAMD), which accounts for most AMD cases, remain limited [2,3]. Current approaches mainly include nutritional supplementation and complement inhibition for geographic atrophy, but these strategies do not directly address the upstream oxidative-inflammatory processes that contribute to RPE degeneration and secondary photoreceptor loss. Therefore, there is a clear need for therapeutic strategies that can intervene in the core pathological cascade of dAMD while maintaining a favorable safety profile.

The RPE is a central therapeutic target for dAMD because its dysfunction is widely recognized as an initiating event in outer retinal degeneration [4]. However, efficient and safe gene delivery to the RPE remains technically challenging. Conventional intravitreal injection is minimally invasive but is limited by the inner limiting membrane and often fails to achieve efficient transduction of the outer retina and RPE [5]. Subretinal injection provides direct access to the RPE, but it requires invasive surgical manipulation and is inherently associated with transient retinal separation, with potential risks of hemorrhage,

* Corresponding author at: Department of Ophthalmology, Beijing Chaoyang Hospital, Capital Medical University, Beijing 100020, PR China.
** Corresponding authors.
E-mail addresses: drfengj@mail.ccmu.edu.cn (J. Feng), wqsun@ipe.ac.cn (W. Sun), taoyong@mail.ccmu.edu.cn (Y. Tao).
[1] Lead contact.

https://doi.org/10.1016/j.jconrel.2026.115289
Received 28 May 2026; Received in revised form 16 August 2026; Accepted 19 August 2026
Available online 24 August 2026

inflammation, or localized retinal injury [6]. These limitations highlight the need for alternative delivery routes that can provide broad RPE access while minimizing iatrogenic damage and systemic exposure.

Delivery into the suprachoroidal space has emerged as a promising route for posterior segment therapy, as it enables anatomical targeting of the choroid-RPE interface without intentional transretinal penetration or subretinal bleb formation [7]. Nevertheless, anatomical targeting alone may not be sufficient for long-term gene therapy. Because sustained AAV-mediated expression can persist for months or longer, promoter-mediated transcriptional control may further improve cell specificity and reduce unnecessary exposure in non-target retinal cells. This is especially important when modulating immune-regulatory pathways, as signaling pathways that contribute to inflammation in the RPE may also support homeostatic or neuroprotective functions in retinal neurons [8–10]. Thus, an optimal ocular gene delivery strategy for dAMD should combine route-based anatomical targeting with promoter-mediated cell-restricted expression.

Mechanistically, dAMD progression is driven by a self-amplifying cycle between oxidative stress and chronic inflammation in the RPE [11–13]. Oxidative injury disrupts RPE homeostasis and activates local immune responses, including microglial/macrophage activation and inflammatory cytokine release [14–16]. Among the inflammatory pathways involved, the Janus kinase/signal transducer and activator of transcription (JAK-STAT) pathway represent a key signaling node [17]. Under physiological conditions, this pathway is restrained by suppressor of cytokine signaling proteins, which act as endogenous negative feedback regulators [18]. Loss of such molecular braking mechanisms may lead to persistent STAT3 activation, thereby amplifying inflammation, mitochondrial dysfunction, oxidative stress, and cell death. Therefore, restoring an endogenous inhibitor of this pathway within the RPE may provide a targeted strategy to interrupt the oxidative-inflammatory loop.

In this study, we first performed transcriptomic analysis of RPE/choroid tissues from a sodium iodate-induced dAMD-like model and cross-validated the findings using a human AMD dataset. This analysis identified SOCS3, a key negative regulator of the JAK-STAT pathway, as a significantly downregulated gene associated with STAT3 hyperactivation and inflammatory amplification in the $NaIO_3$-induced model. Based on this finding, we designed a dual-restricted AAV gene delivery system that combines suprachoroidal administration for anatomical RPE access with an RPE-specific Best1 promoter for transcriptional restriction. We then evaluated the route-dependent transduction profile, RPE-restricted expression, biodistribution, long-term expression, therapeutic efficacy, and ocular/systemic safety of AAV-Best1-SOCS3 [19,20]. Through this approach, we sought to establish a controlled and targeted ocular gene delivery platform for localized SOCS3 restoration and modulation of oxidative-inflammatory retinal degeneration.

2. Results

2.1. Transcriptomic profiling reveals SOCS3 downregulation and JAK-STAT pathway activation in $NaIO_3$-induced dAMD-like retinal injury

To explore the molecular alterations associated with dAMD, we performed bulk RNA sequencing on RPE/choroid complexes harvested from $NaIO_3$-treated mice and normal controls (Fig. 1A). Differential expression analysis identified a total of 1515 differentially expressed genes (DEGs), comprising 459 upregulated and 1056 downregulated genes in the $NaIO_3$-induced injury group compared to the normal group (Fig. 1B). Among the most significantly changed genes, several downregulated genes included *Bcl3, Timp1*, and *Socs3*, while upregulated genes included *Rpe65, Slc16a8,* and *Rabgef1* (Fig. 1B). To explore the functional relationships among these DEGs, we constructed a protein-protein interaction (PPI) network, which highlighted a subset of hub genes with high connectivity, including Socs3 and Stat3 (Fig. 1C). Gene Ontology (GO) enrichment analysis revealed that the DEGs were predominantly enriched in biological processes related to immune and inflammatory responses, such as “immune response” and “response to cytokine” (Fig. 1D). Gene Set Enrichment Analysis (GSEA) further demonstrated that several critical signaling pathways were significantly enriched in the $NaIO_3$-induced dAMD-like phenotype, including the IL-17 signaling pathway, apoptosis, NF-κB signaling pathway, and the JAK-STAT signaling pathway (Fig. 1E). Given that SOCS3 encodes a key negative regulator of cytokine signaling and serves as a central feedback inhibitor of the JAK-STAT pathway, its significant downregulation—coupled with the positive enrichment of the JAK-STAT pathway—suggested a potential loss of negative feedback control that may contribute to exacerbated inflammation in dAMD (Table S1).

To corroborate our *in vivo* transcriptomic findings and evaluate their clinical relevance, we analyzed the public human dataset GSE99248, which comprises RPE/choroid/scleral complexes from AMD patients and healthy individuals (Fig. 1F). Consistent with our murine model, differential expression analysis of this clinical cohort confirmed a marked downregulation of *SOCS3* in AMD samples (Fig. 1G). Analysis of individual sample values further showed reduced SOCS3 expression in AMD samples compared with normal controls (Fig. 1H), underscoring the potential clinical significance of SOCS3 deficiency in AMD pathogenesis. The AMD samples in this dataset included different disease stages, including early AMD and late-stage AMD related samples according to the available clinical annotations. SOCS3 expression was broadly reduced across the annotated AMD samples compared with normal controls, supporting disease-associated SOCS3 downregulation in human AMD samples.

To validate these transcriptomic findings at the protein level, we assessed the pathological changes and inflammatory status in the $NaIO_3$-treated mice model (Fig. 1I). Immunofluorescence staining of retina sections confirmed a marked decrease in SOCS3 content within the RPE layer of $NaIO_3$-treated mice compared to normal controls (Fig. 1J). Quantitative analysis of immunofluorescence intensity further revealed a marked reduction of SOCS3 fluorescence intensity between the RPE and the neural retina (Fig. S1A). Consistent with activation of the JAK-STAT pathway, p-STAT3 levels were increased in $NaIO_3$-treated mice retinal sections (Fig. 1K), as confirmed by quantitative fluorescence analysis (Fig. S1B). Moreover, this signaling imbalance coincided with pronounced microglial activation, as evidenced by increased IBA1 immunoreactivity (Fig. 1L) and its concomitant quantitative upregulation (Fig. S1C). This profound cellular stress translated into a highly pro-inflammatory microenvironment, as evidenced by significantly elevated concentrations of IL-1β, IL-6, TNF-α, and IFN-γ in RPE/choroid homogenates (Fig. 1M). Collectively, these data indicate that in the $NaIO_3$-induced dAMD-like model, SOCS3 downregulation is associated with inflammatory activation and increased STAT3 phosphorylation.

2.2. Restoration of SOCS3 attenuates inflammation and oxidative injury in vitro

To evaluate the therapeutic potential of SOCS3 in a controlled environment, we established a model by exposing human retinal pigment epithelium (ARPE-19) cells to hydrogen peroxide (H_2O_2) stimulation (Fig. 2A) [21]. Immunofluorescence staining and flow cytometry confirmed efficient overexpression of 3flag-tagged SOCS3 (Fig. 2B and Fig. S2A). Furthermore, while H_2O_2 treatment markedly upregulated p-STAT3 in the PBS control, this activation was effectively suppressed by SOCS3 overexpression (Fig. 2C and Fig. S2B).

Consequently, SOCS3 restoration significantly suppressed the inflammatory response. ELISA analysis revealed that the pro-inflammatory cytokines (IL-1β, IL-6, TNF-α, and IFN-γ) induced by H_2O_2 were significantly attenuated in the SOCS3-overexpressing cells (Fig. 2D). Because oxidative-inflammatory stress is closely linked to mitochondrial injury, we next evaluated mitochondrial integrity. Immunofluorescence staining of the mitochondrial outer membrane

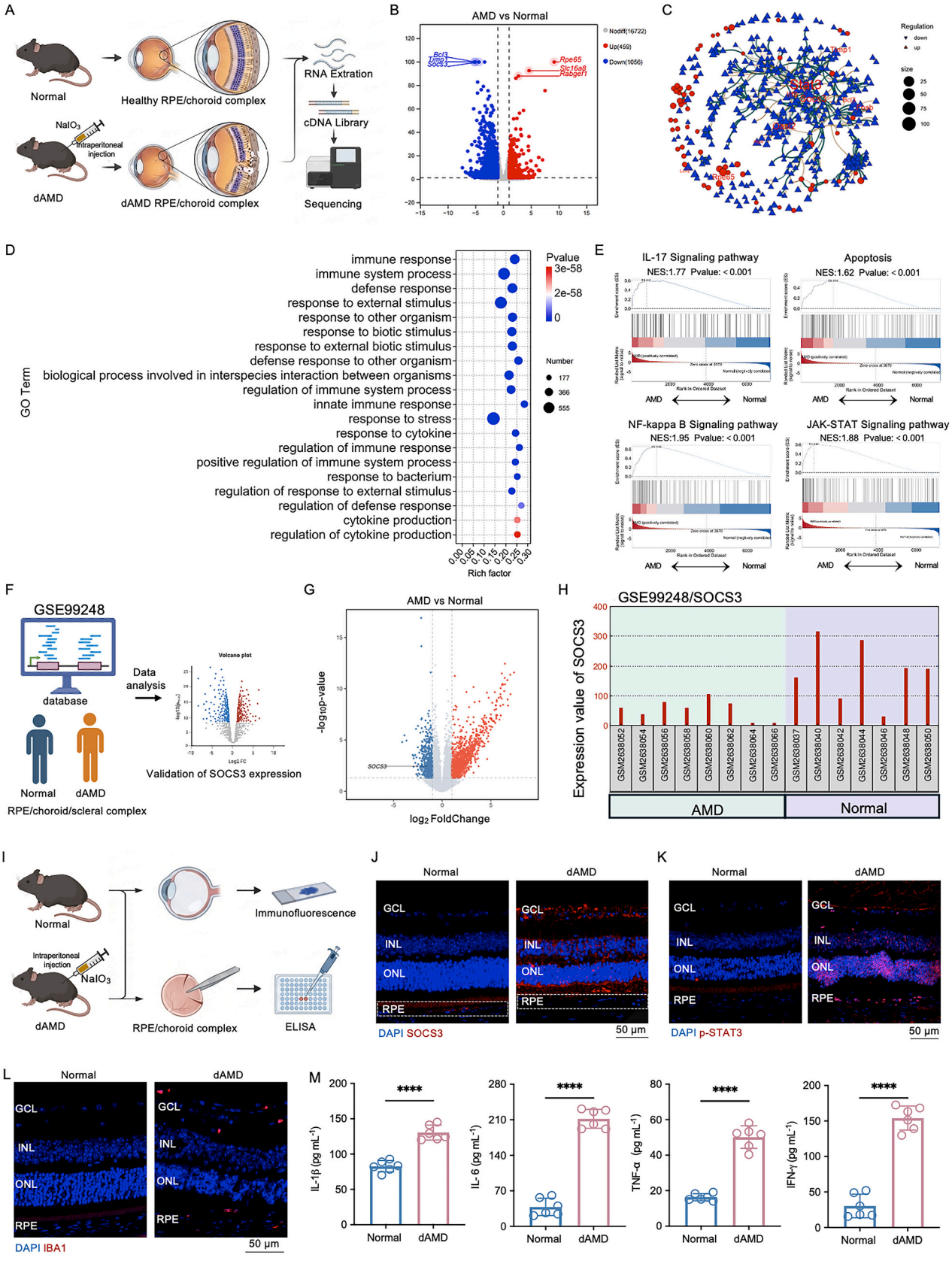

(caption on next page)

Fig. 1. Transcriptomic analysis reveals dysregulation of the SOCS3-STAT3 axis and exacerbated inflammation in $NaIO_3$-induced dAMD-like retinal injury.
(A) Schematic workflow of the experimental design. RPE/choroid complexes were harvested from $NaIO_3$-treated mice and normal controls for bulk RNA sequencing.
(B) Volcano plot of differentially expressed genes (DEGs). Red and blue dots represent significantly upregulated and downregulated genes, respectively.
(C) Protein-protein interaction (PPI) network of core DEGs, with node size indicating connectivity degree.
(D) Gene Ontology (GO) enrichment analysis showing biological processes significantly enriched in $NaIO_3$-treated tissues, predominantly highlighting immune and inflammatory responses.
(E) Gene Set Enrichment Analysis (GSEA) plots identifying key signaling pathways activated in $NaIO_3$-induced dAMD-like model, including IL-17, Apoptosis, NF-κB, and JAK-STAT.
(F) Schematic workflow for bioinformatic validation of SOCS3 expression using the human GSE99248 dataset.
(G) Volcano plot of the GSE99248 dataset identifying the downregulation of SOCS3 in clinical AMD samples.
(H) Individual expression values of SOCS3 comparing AMD patients to normal controls in the GSE99248 cohort.
(I) Schematic workflow for experimental validation of transcriptomic targets.
(J-L) Representative immunofluorescence images of SOCS3 (J), p-STAT3 (K) and the microglia/macrophage marker IBA1 (L) in retinal sections. Nuclei were counterstained with DAPI (blue). GCL, ganglion cell layer; INL, inner nuclear layer; ONL, outer nuclear layer; RPE, retinal pigment epithelium. White dashed boxes indicate the retinal pigment epithelium (RPE) layer. All images share the same scale bars.
(M) Quantification of pro-inflammatory cytokines (IL-1β, IL-6, TNF-α, IFN-γ) in RPE/choroid complex homogenates by ELISA. ($n = 6$ biologically independent samples).
Data in M are presented as mean ± SD and were compared *via* two tailed unpaired Student's *t*-test. ****$p < 0.0001$. (For interpretation of the references to colour in this figure legend, the reader is referred to the web version of this article.)

protein TOM20 revealed severe mitochondrial network fragmentation and loss of mass following H_2O_2 insult. Remarkably, SOCS3 restoration partially preserved mitochondrial morphology and TOM20 fluorescence intensity (Fig. 2E and Fig. S2C). This preservation was vividly corroborated at the ultrastructural level using transmission electron microscopy (TEM), while PBS-treated cells exhibited swollen mitochondria with severely disrupted cristae, SOCS3-treated cells maintained relatively better-preserved mitochondrial ultrastructure (Fig. 2F). Consistent with the TOM20 and TEM findings, JC-1 staining further showed that H_2O_2 exposure reduced mitochondrial membrane potential, as indicated by increased JC-1 monomer fluorescence and decreased aggregate fluorescence. SOCS3 restoration partially rescued H_2O_2-induced mitochondrial membrane potential loss, providing functional support for its mitochondrial protective effect (Fig. S3). Furthermore, restoring mitochondrial function translated to a marked reduction in intracellular ROS accumulation (Fig. 2G, quantified in Fig. S2D).

Importantly, alleviating this intracellular stress cascade preserved fundamental RPE cellular characteristics and barrier functions. The SOCS3 treatment group maintained expression of the vital RPE65 (Fig. 2H, Fig. S2E) and the tight junction protein ZO-1, ensuring the integrity of the epithelial monolayer (Fig. 2I, Fig. S2F). SOCS3 restoration also reduced H_2O_2-induced apoptosis and cell death, as evidenced by Calcein-AM/PI double staining (Fig. 2J). Collectively, these *in vitro* results demonstrate that AAV-mediated SOCS3 delivery effectively protects RPE cells against oxidative injury by suppressing inflammation, reducing ROS accumulation, and preserving vital mitochondrial and barrier functions.

2.3. STAT3 inhibition partially rescues oxidative-inflammatory RPE injury aggravated by SOCS3 deficiency

To further determine whether excessive STAT3 activation contributes to the aggravated RPE injury caused by SOCS3 deficiency, we performed SOCS3 loss-of-function and Stattic rescue experiments in ARPE-19 cells. Cells were transfected with siNC or siSOCS3 at 0 h, followed by H_2O_2 stimulation at 48 h where indicated. In the rescue group, Stattic was administered together with H_2O_2, and cells were collected at 54 h for evaluation (Fig. S4A).

qPCR analysis confirmed efficient SOCS3 knockdown in both siSOCS3 and H_2O_2 + siSOCS3 groups. SOCS3 mRNA remained markedly reduced in the H_2O_2 + siSOCS3 + Stattic group and did not differ significantly from the H_2O_2 + siSOCS3 group, indicating that Stattic did not restore SOCS3 expression (Fig. S4B). SOCS3 knockdown increased p-STAT3 immunoreactivity under basal conditions and further enhanced H_2O_2-induced STAT3 activation (Fig. S4C). This was accompanied by increased ROS accumulation, TOM20 disruption, ZO-1 loss, and increased cell death (Fig. S4D, E, F and G).

Notably, Stattic reduced p-STAT3 activation and partially attenuated ROS accumulation, mitochondrial disruption, ZO-1 loss, and cell death in SOCS3-deficient cells under H_2O_2-induced oxidative stress. These findings suggest that excessive STAT3 activation contributes, at least in part, to the oxidative-inflammatory RPE injury aggravated by SOCS3 deficiency. Together, these loss-of-function results support reduced SOCS3 as a functional contributor to oxidative-inflammatory RPE injury rather than a stand-alone initiator of dAMD-like pathology.

2.4. SOCS3 restoration after injury initiation attenuates prolonged $NaIO_3$-induced oxidative-inflammatory RPE injury

To further assess whether SOCS3 restoration remains protective under sustained oxidative stress after injury initiation, we established a prolonged $NaIO_3$-induced RPE dysfunction model in ARPE-19 cells. Cells were exposed to 5 mM $NaIO_3$ from Day 0 to Day 5. To avoid a prophylactic treatment design, PBS or AAV-CMV-SOCS3-3flag was administered on Day 2 after injury had already been initiated, while $NaIO_3$ exposure was continued until Day 5 (Fig. S5A).

AAV-CMV-SOCS3-3flag successfully restored SOCS3 expression, as confirmed by 3flag immunofluorescence (Fig. S5B). Prolonged $NaIO_3$ exposure increased p-STAT3 immunoreactivity, ROS accumulation, TOM20-labeled mitochondrial disruption, ZO-1 loss, cell death, and inflammatory cytokine production, including IL-1β, IL-6, TNF-α, and IFN-γ. SOCS3 restoration after injury initiation attenuated p-STAT3 activation, reduced ROS accumulation and inflammatory cytokine production, partially preserved TOM20 and ZO-1 expression, and improved cell viability (Fig. S5C, D, E, F, G and H). These findings suggest that SOCS3-mediated protection can also be observed under prolonged oxidative RPE stress after injury initiation.

2.5. Suprachoroidal administration improves AAV access to the RPE compared with intravitreal delivery

To compare the effects of administration route on RPE access and retinal distribution, we evaluated intravitreal, suprachoroidal, and subretinal delivery. Subretinal injection was included as a route-comparison control rather than as the primary strategy because it requires transretinal access and formation of a transient subretinal bleb [22]. IVT administration resulted in a predominantly inner-retinal transduction pattern. Specifically, IVT delivery of AAV-CMV-SOCS3-EGFP targeted the retinal ganglion cell layer (GCL) and the inner nuclear layer (INL) but largely failed to penetrate the inner limiting membrane to reach the RPE (Fig. 3A, B). In contrast, SCS delivery markedly enhanced transgene expression in the RPE layer, although weak off-target expression was still detectable in adjacent retinal layers when driven by the CMV promoter. (Fig. 3C, D). Because subretinal

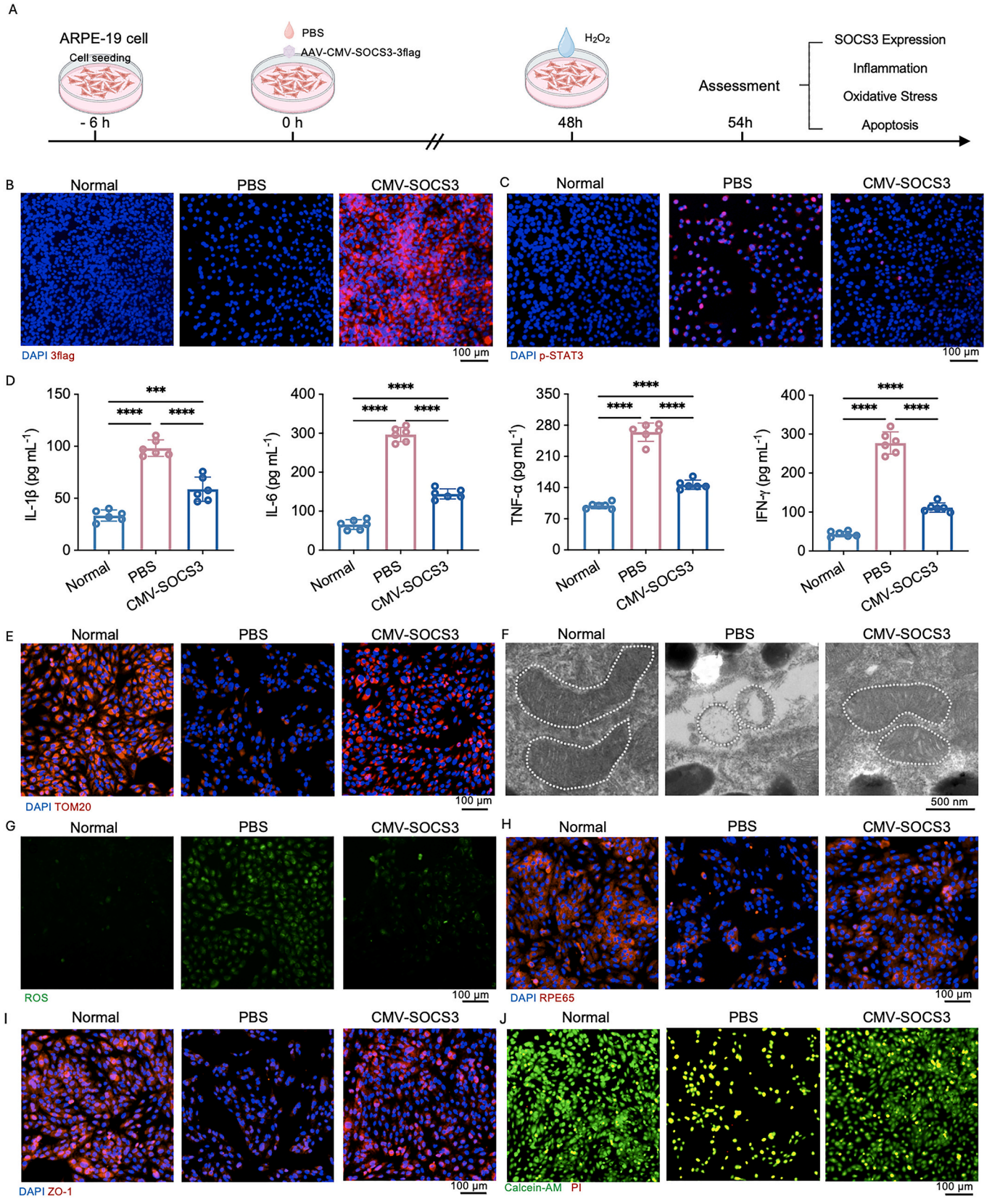

(caption on next page)

Fig. 2. Restoration of SOCS3 mitigates inflammation, oxidative stress, and apoptosis *in vitro*.
(A) Schematic illustration of the *in vitro* experimental design. ARPE-19 cells were incubated with PBS or AAV-CMV-SOCS3-3flag for 48 h prior to H_2O_2 stimulation (6 h).
(B, C) Representative immunofluorescence images showing the restoration of 3flag (B) and the suppression of p-STAT3 (C). Nuclei were stained with DAPI (blue). All images share the same scale bars.
(D) Quantification of pro-inflammatory cytokines (IL-1β, IL-6, TNF-α, IFN-γ) in cell culture supernatants by ELISA ($n = 6$ biologically independent samples).
(E) Immunofluorescence staining of the mitochondrial marker TOM20 (red). Nuclei were stained with DAPI (blue). All images share the same scale bars.
(F) Representative TEM images showing mitochondrial morphology. All images share the same scale bars.
(G) Assessment of intracellular ROS levels using DCFH-DA staining (green). Nuclei were stained with DAPI (blue). All images share the same scale bars.
(H, I) Immunofluorescence staining of the RPE cell marker RPE65 (H, red) and the tight junction protein ZO-1 (I, red), indicating the preservation of RPE characteristics and epithelial barrier function. Nuclei were stained with DAPI (blue). All images share the same scale bars.
(J) Cell viability analyzed by Calcein-AM (green, live cells) and PI (red, dead cells) double staining. All images share the same scale bars.
Data in D are presented as mean ± SD and were compared *via* One-Way ANOVA. ***$p < 0.001$, ****$p < 0.0001$. (For interpretation of the references to colour in this figure legend, the reader is referred to the web version of this article.)

injection is an established and efficient route for direct RPE access, we included subretinal administration as a route-comparison control (Fig. S6A). Subretinal injection of AAV-CMV-SOCS3-EGFP produced robust local transgene expression in the outer retina/RPE-adjacent region, confirming its strong ability to access the RPE/outer retina (Fig. S6B). These findings support subretinal injection as a highly efficient route for direct outer retina/RPE access. However, subretinal delivery generally requires access to the subretinal space and creation of a transient subretinal bleb, which has been associated with localized retinal separation, retinal manipulation, reflux, or other procedure-related complications in previous studies [23].

Together, these route-comparison experiments show that intravitreal delivery has limited access to the RPE, whereas suprachoroidal administration improves AAV delivery toward the choroid-RPE interface without intentional transretinal penetration or the need to create a subretinal bleb under the tested conditions. Therefore, suprachoroidal delivery provides an anatomical basis for RPE-oriented gene delivery, while additional promoter-mediated transcriptional control is required to further restrict transgene expression to RPE cells.

2.6. Best1 promoter-mediated transcriptional restriction enables durable RPE-localized expression

To achieve targeted *in vivo* gene delivery, AAV-Best1-SOCS3-EGFP was administered to mice *via* suprachoroidal injection (Fig. 3E). Immunofluorescence analysis showed that EGFP expression was predominantly localized to the RPE layer, with limited detectable signal in adjacent neural retinal layers (Fig. 3F). To further assess the advantage of Best1-mediated transcriptional restriction, we compared SOCS3-EGFP expression driven by the non-RPE-specific CMV promoter and the RPE-specific Best1 promoter after suprachoroidal delivery at equivalent vector doses. AAV-CMV-SOCS3-EGFP produced broader expression in the outer retina/RPE region, with detectable EGFP signal extending beyond the RPE layer. In contrast, AAV-Best1-SOCS3-EGFP expression was mainly confined to the RPE layer, with reduced neural retinal off-target expression. These findings support the use of the Best1 promoter to achieve more RPE-confined SOCS3 expression after suprachoroidal AAV administration.

Because broader transgene expression may increase unnecessary SOCS3 exposure in neural retinal cells, we further evaluated retinal apoptosis one month after AAV-CMV-SOCS3-3flag or AAV-Best1-SOCS3-3flag administration. TUNEL staining showed more TUNEL-positive signals in the AAV-CMV-SOCS3-3flag group, whereas AAV-Best1-SOCS3-3flag administration resulted in fewer TUNEL-positive cells under the same conditions (Fig. S7). These findings support the rationale for using Best1-mediated transcriptional restriction to reduce potential neural retinal off-target effects after suprachoroidal AAV-SOCS3 delivery.

To further characterize the dose-expression relationship of AAV-Best1-SOCS3-3flag and provide additional experimental support for the selected working dose, mice received suprachoroidal administration of the vector at 5×10^9, 1×10^{10}, 2×10^{10}, and 4×10^{10} vg/eye. Transgene-derived SOCS3 expression was evaluated by 3flag immunofluorescence in the RPE at 1 month after administration. RPE 3flag expression increased progressively from 5×10^9 to 2×10^{10} vg/eye. In contrast, increasing the dose to 4×10^{10} vg/eye did not produce a further significant increase compared with 2×10^{10} vg/eye (Fig. S8). These findings indicate that RPE transgene expression approached a plateau at 2×10^{10} vg/eye within the tested dose range and support this dose as the lowest tested dose achieving near-maximal RPE transgene expression.

To evaluate the *in vivo* performance of our optimized approach, we investigated the biodistribution and long-term stability of transgene expression following suprachoroidal injection. We employed a luciferase reporter vector driven by the Best1 promoter (AAV-Best1-SOCS3-Luciferase) to dynamically monitor expression kinetics (Fig. 3G). *Ex vivo* bioluminescence imaging at one-month post injection demonstrated that the expression was highly confined to the injected eye, with negligible background signals in major systemic organs (heart, liver, spleen, lung, kidney, and brain). This confirms the superior ocular specificity and the minimization of potential systemic safety risks of the suprachoroidal space delivery route combined with an RPE-specific promoter (Fig. 3H, I).

To further assess systemic vector dissemination, WPRE sequences were quantified by qPCR in the injected eye and major organs. After normalization to β-actin, the relative WPRE signal was predominantly enriched in the injected eye, whereas only minimal signals were detected in the heart, liver, spleen, lung, kidney, and brain. These results were consistent with the *ex vivo* bioluminescence imaging data and further supported the ocular-localized biodistribution of the suprachoroidally delivered AAV-Best1-SOCS3-3flag vector (Fig. S9). Furthermore, *in vivo* imaging revealed bioluminescence persisted for at least six months post injection (Fig. 3J, K). These data indicate that a single suprachoroidal administration of the engineered AAV vector can achieve targeted and sustained ocular expression with limited off-target signal.

2.7. Suprachoroidal delivery of AAV-Best1-SOCS3-3flag preserves retinal architecture in vivo

Having established the protective role of SOCS3 *in vitro*, we next evaluated its therapeutic efficacy in a $NaIO_3$-induced dAMD mouse model [24]. Given the limitations of the $NaIO_3$-induced model, which triggers rapid and severe RPE injury and does not fully recapitulate the slow progression of human disease [25,26], and considering that AAV-mediated transgene expression in the mouse retina reaches its peak approximately one month after administration [27], we administered AAV-Best1-SOCS3-3flag prophylactically *via* suprachoroidal injection one month prior to $NaIO_3$ challenge (Fig. 4A), a widely adopted strategy in preclinical AAV studies to ensure adequate transgene expression before disease onset. Immunofluorescence analysis of the retina confirmed that this targeted approach successfully restored SOCS3 expression predominantly in the RPE (Fig. 4B). Consequently, this

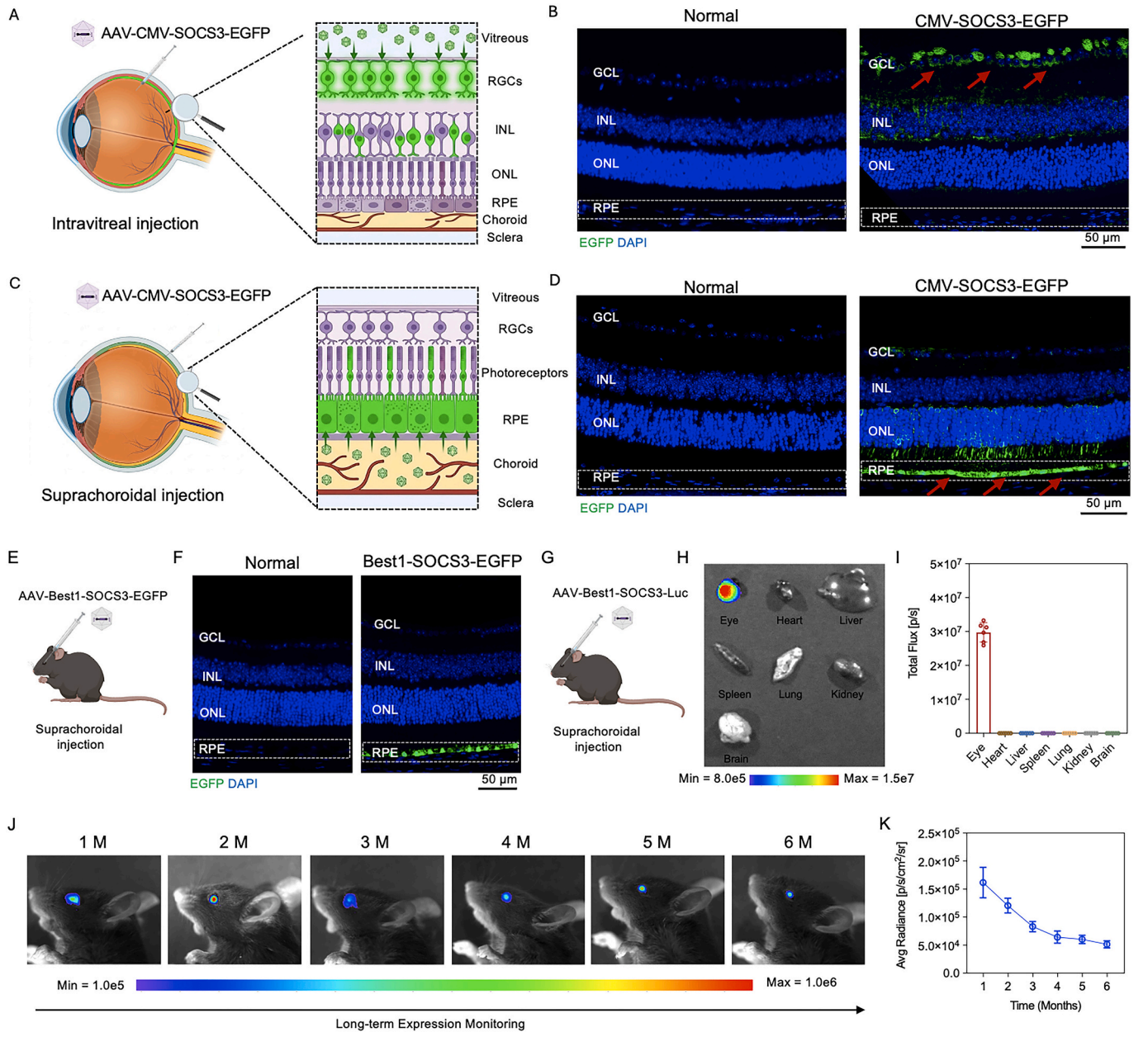

Fig. 3. Suprachoroidal delivery of AAV-Best1-SOCS3 achieves targeted, safe, and sustained transgene expression in the RPE.
(A) Schematic illustration of IVT injection of AAV-CMV-SOCS3-EGFP into the vitreous chamber.
(B) Representative fluorescence images of retinal sections following IVT injection, showing transduction predominantly in the inner retina (red arrows) with negligible expression in the RPE. Nuclei were stained with DAPI (blue). GCL, ganglion cell layer; INL, inner nuclear layer; ONL, outer nuclear layer; RPE, retinal pigment epithelium. White dashed boxes indicate the RPE layer. All the images share the same scale bars.
(C) Schematic illustration of SCS injection of AAV-CMV-SOCS3-EGFP. The vector is delivered into the potential space between the sclera and choroid.
(D) Representative fluorescence images following SCS injection, showing transgene expression predominantly localized to the RPE layer (red arrows). Nuclei were stained with DAPI (blue). GCL, ganglion cell layer; INL, inner nuclear layer; ONL, outer nuclear layer; RPE, retinal pigment epithelium. White dashed boxes indicate the RPE layer. All the images share the same scale bars.
(E) Schematic illustration of AAV-Best1-SOCS3-EGFP delivery *via* suprachoroidal injection.
(F) Representative immunofluorescence images showing EGFP expression predominantly localized to the RPE layer. Nuclei were stained with DAPI (blue). GCL, ganglion cell layer; INL, inner nuclear layer; ONL, outer nuclear layer; RPE, retinal pigment epithelium. White dashed boxes indicate the RPE layer. All the images share the same scale bars.
(G) Schematic of the experimental design for assessing organ-specific biodistribution and long-term expression after SCS injection of AAV-Best1-SOCS3-Luciferase.
(H) Representative *ex vivo* bioluminescence images of harvested organs (eye, heart, liver, spleen, lung, kidney, and brain), showing predominant localization of the bioluminescence signal to the injected eye, with minimal detectable signal in major systemic organs.
(I) Quantification of the total flux from the harvested organs shown in (H).
(J) Representative longitudinal *in vivo* bioluminescence images of mouse eyes from 1 to 6 months (1 M–6 M) post-injection.
(K) Quantification of the average radiance from the region of interest (ROI) over the eye across the 6-month timeline, demonstrating stable and sustained transgene expression. ($n = 6$ biologically independent samples).
Data in I and K are presented as mean ± SD. (For interpretation of the references to colour in this figure legend, the reader is referred to the web version of this article.)

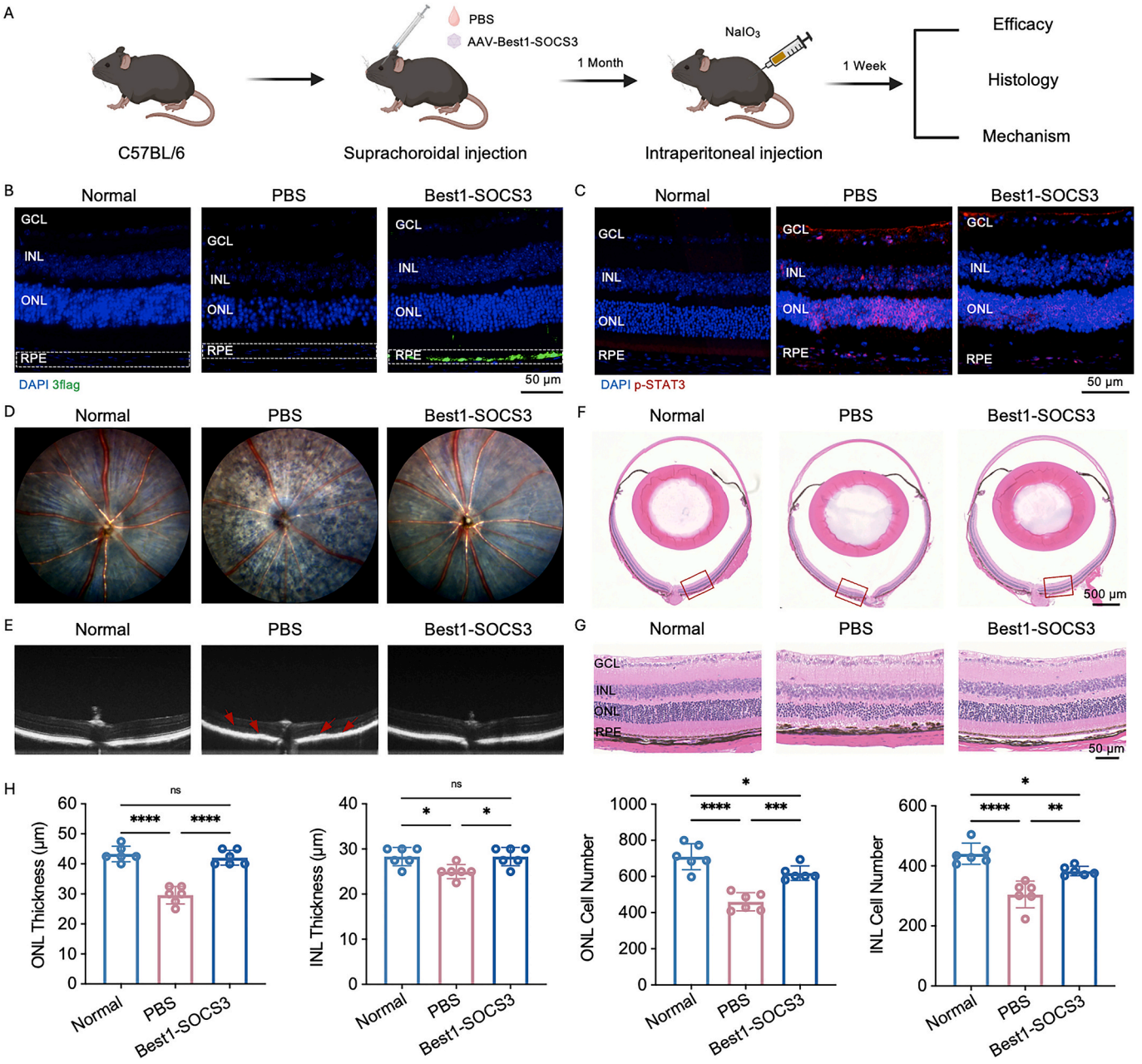

Fig. 4. Suprachoroidal delivery of AAV-Best1-SOCS3 preserves retinal morphology and photoreceptor survival *in vivo*.
(A) Schematic illustration of the experimental timeline. C57BL/6 mice received a prophylactic suprachoroidal injection of PBS or AAV-Best1-SOCS3-3flag one month prior to $NaIO_3$-induced retinal injury, followed by evaluation after 1 week.
(B, C) Representative immunofluorescence images assessing the expression of 3flag (B, green) and p-STAT3 (C, red) in the retina. Nuclei were stained with DAPI (blue). White dashed boxes indicate the RPE layer. All the images share the same scale bars.
(D) Representative *in vivo* fundus imaging. PBS-treated mice exhibited severe retinal spotting and pigmentary changes indicative of profound RPE damage, which were effectively prevented in the Best1-SOCS3 group.
(E) Representative *in vivo* OCT imaging. Red arrows highlight the collapse and disorganization of the outer retinal layers in the PBS group, whereas the Best1-SOCS3 group showed preserved retinal lamination.
(F, G) Representative H&E staining of whole eye globes (F) and magnified images (G) corresponding to the red boxed areas, illustrating the structural preservation of retinal layers following gene therapy. GCL, ganglion cell layer; INL, inner nuclear layer; ONL, outer nuclear layer; RPE, retinal pigment epithelium. All the images of F share the same scale bars, and all the images of G share the same scale bars.
(H) Quantitative analysis of ONL and INL thickness, as well as the respective nuclei counts, demonstrating a significant rescue of photoreceptor layers by Best1-SOCS3 ($n = 6$ biologically independent animals).
Data in H are presented as mean ± SD and were analyzed *via* One-Way ANOVA. ns, not significant; $^{*}p < 0.05$, $^{**}p < 0.01$, $^{***}p < 0.001$, $^{****}p < 0.0001$. (For interpretation of the references to colour in this figure legend, the reader is referred to the web version of this article.)

restoration significantly suppressed the pathological elevation of p-STAT3 observed in AAV-Best1-SOCS3-3flag treated $NaIO_3$-induced injury group, which was further corroborated by quantitative fluorescence density analysis (Fig. 4C and Fig. S11A).

To assess the *in vivo* therapeutic effects on retinal morphology, non-invasive ocular imaging was performed. Fundus photography revealed that PBS-treated mice exhibited severe retinal damage, characterized by diffuse patchy hypopigmentation and spotting indicative of profound RPE atrophy. Similarly, mice administered with the empty vector control (AAV-Best1-Null) also exhibited severe retinal degeneration with pronounced mottling and structural deterioration (Fig. S10A). In contrast, retinas treated with AAV-Best1-SOCS3-3flag showed fewer pigmentary abnormalities and a more preserved fundus appearance than PBS-treated eyes (Fig. 4D). Furthermore, optical coherence tomography (OCT) imaging showed that $NaIO_3$ administration caused marked retinal thinning, collapse, and severe disruption of the hyperreflective outer retinal bands corresponding to the photoreceptor and RPE layers (red arrows). A similar pathological phenotype was observed in the Best1-

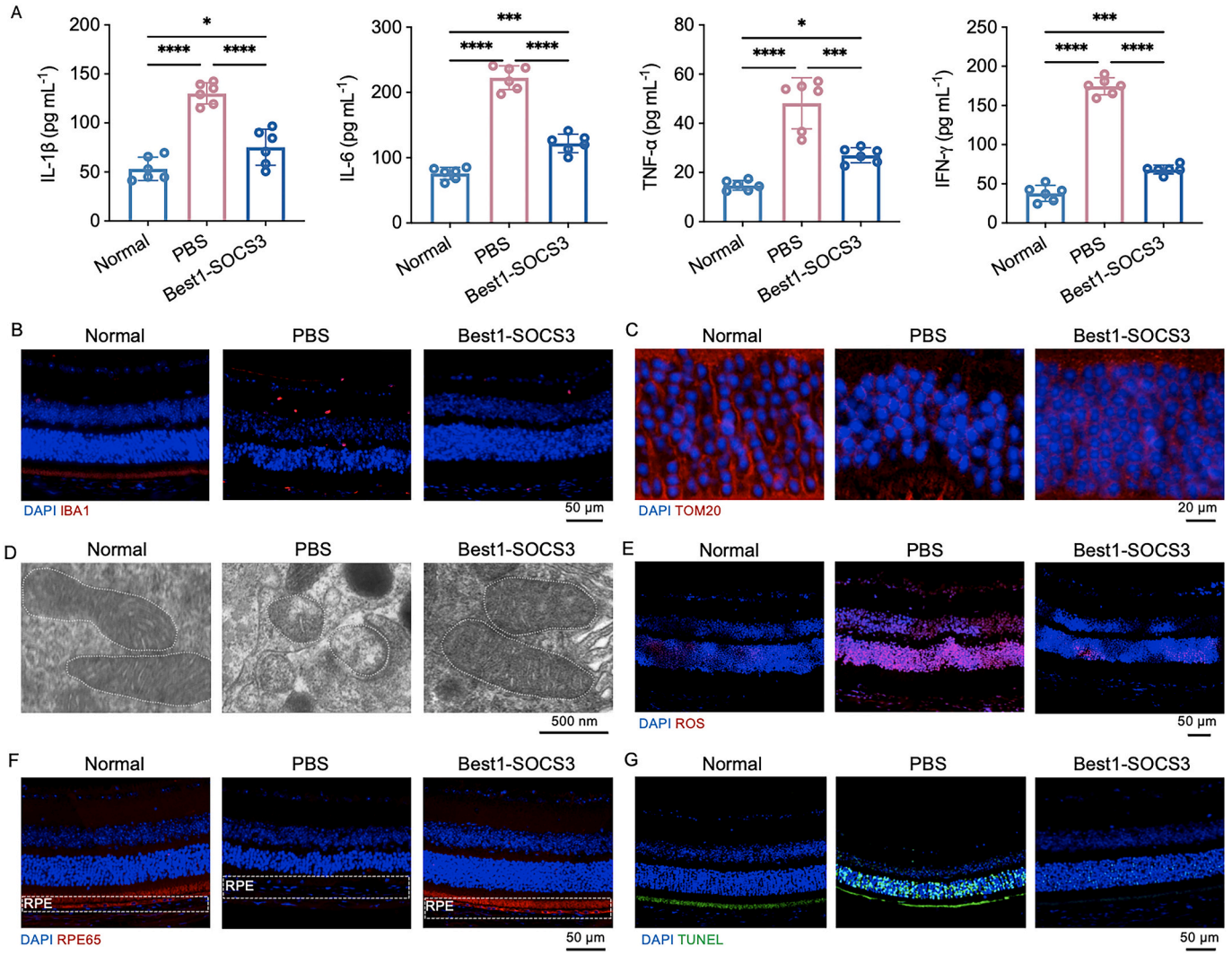

Fig. 5. AAV-Best1-SOCS3 alleviates inflammation, oxidative stress, and apoptosis *in vivo*.
(A) Quantification of pro-inflammatory cytokines (IL-1β, IL-6, TNF-α, IFN-γ) in RPE/Choroid complex homogenates by ELISA, demonstrating an obvious suppression of the inflammatory storm following SOCS3 gene therapy. ($n = 6$ biologically independent samples).
(B) Representative immunofluorescence images of IBA1 (red, a marker for microglia/macrophage) in retinal sections, showing reduced pathological activation and subretinal infiltration in the SOCS3-treated group. Nuclei were stained with DAPI (blue). All images share the same scale bars.
(C) Immunofluorescence staining of the mitochondrial marker TOM20 (red), indicating mitochondrial network integrity. Nuclei were stained with DAPI (blue). All images share the same scale bars.
(D) Representative TEM images showing the ultrastructure and morphology of mitochondria. Note the preserved morphology with well-defined cristae in the Best1-SOCS3 group, contrasting with the severely swollen and vacuolated mitochondria in the PBS group. All images share the same scale bars.
(E) *In situ* detection of retinal ROS levels using fluorescent staining (red), revealing abated oxidative stress upon treatment. Nuclei were stained with DAPI (blue). All images share the same scale bars.
(F) Representative immunofluorescence images of RPE65 (red), demonstrating the obvious maintenance of RPE specific function and survival. Nuclei were stained with DAPI (blue). White dashed boxes indicate the RPE layer. All images share the same scale bars.
(G) Assessment of retinal cell apoptosis using the TUNEL assay (green), showing obvious prevention of cell death in the outer retina. Nuclei were stained with DAPI (blue). All images share the same scale bars.
In the figure panels and quantitative plots, "Best1-SOCS3" denotes the group treated with AAV-Best1-SOCS3-3flag. Data in A are presented as mean ± SD and were compared *via* One-Way ANOVA. $*p < 0.05$, $***p < 0.001$, $****p < 0.0001$. (For interpretation of the references to colour in this figure legend, the reader is referred to the web version of this article.)

Null control group (Fig. S10B). In contrast, Best1-SOCS3 treatment partially preserved retinal lamination and reduced outer retinal disruption (Fig. 4E). Histological analysis with H&E staining provided quantitative assessment of these structural improvements. In the PBS-treated group, a noticeable reduction in outer nuclear layer (ONL) thickness and widespread loss of photoreceptor nuclei were observed, suggesting considerable photoreceptor degeneration following RPE injury. In contrast, the Best1-SOCS3 group displayed well-preserved retinal lamination, with maintained structure in both the ONL and INL (Fig. 4F, G). Morphometric measurements further supported these findings: treatment with Best1-SOCS3 led to significantly greater ONL and INL thicknesses and higher nuclei counts compared with the vehicle group. Notably, while the overall thicknesses of the ONL and INL in treated mice showed no significant difference from healthy normal controls, the corresponding nuclei count demonstrated only partial restoration (Fig. 4H). These results suggest that the targeted gene therapy helped stabilize the retinal layered architecture and attenuated photoreceptor loss, offering protective effects against oxidative stress induced retinal degeneration.

2.8. AAV-Best1-SOCS3 gene therapy ameliorates inflammation and oxidative stress

We next assessed the downstream cellular and molecular effects of AAV-Best1-SOCS3-3flag treatment *in vivo*. Given the critical role of the SOCS3-STAT3 axis in immune regulation, we first evaluated the inflammatory microenvironment. ELISA analysis of RPE/choroid homogenates confirmed that local overexpression of SOCS3 in the RPE significantly attenuated the $NaIO_3$-induced storm of key pro-inflammatory cytokines, including IL-1β, IL-6, TNF-α, and IFN-γ (Fig. 5A). Consistent with this data, immunostaining for IBA1 revealed that Best1-SOCS3 treatment significantly dampened the pathological activation and subretinal infiltration of microglia/macrophages, which were highly prevalent in the PBS-treated controls (Fig. 5B and Fig. S11B).

Crucially, the suppression of inflammation was tightly accompanied by the preservation of vital cellular organelles. At the subcellular level, SOCS3 restoration effectively prevented mitochondrial fragmentation, as indicated by a more intact and less disrupted TOM20 mitochondrial network in retinal sections (Fig. 5C and Fig. S11C). This protective effect was further substantiated by TEM. Ultrastructural analysis revealed that Best1-SOCS3 preserved intact mitochondrial morphology with well-defined cristae, in contrast to the severely swollen and vacuolated mitochondria with disrupted internal structures observed in the $NaIO_3$-induced injury group (Fig. 5D). Furthermore, Best1-SOCS3 treatment reduced $NaIO_3$-induced oxidative stress, as indicated by decreased ROS accumulation in retinal sections (Fig. 5E and Fig. S11D).

Consequently, the mitigation of inflammatory and oxidative damage helped preserve essential RPE-specific features, as indicated by the maintenance of the RPE65, which was reduced in the vehicle-treated group (Fig. 5F and Fig. S11E). Ultimately, this restoration of cellular homeostasis was associated with improved cell survival. TUNEL staining showed less apoptosis, with fewer positive cells in the ONL of SOCS3-treated mice compared to the control group (Fig. 5G and Fig. S11F). Taken together, these findings suggest that Best1-SOCS3 may attenuate the oxidative-inflammatory cascade, thereby contributing to the preservation of mitochondrial integrity, RPE function, and photoreceptor survival.

2.9. Comprehensive safety profile of suprachoroidal AAV-Best1-SOCS3

Based on the dose-ranging analysis, 2×10^{10} vg/eye was selected as the lowest tested dose achieving near-maximal RPE transgene expression. We therefore subjected this working dose to comprehensive ocular and systemic safety evaluation following suprachoroidal administration of AAV-Best1-SOCS3-3flag. Ocular compatibility was first evaluated by non-invasive imaging. Fundus photography showed that the Best1-SOCS3 injected eyes were indistinguishable from normal eyes, exhibiting no signs of retinal detachment, hemorrhage, or pigmentary abnormalities (Fig. 6A). Similarly, OCT imaging confirmed the preservation of normal retinal lamination and thickness, with no evidence of edema or structural disruption (Fig. 6B). Furthermore, intraocular pressure (IOP), a critical safety parameter, remained within the physiological range with no significant difference observed between the treated and normal groups (Fig. 6C). To evaluate retinal functional integrity, electroretinography (ERG) was performed. As shown in Fig. S12A, Best1-SOCS3 treated eyes exhibited representative ERG waveforms comparable to those of the contralateral normal eyes. Quantitative analysis further showed that neither the absolute a-wave amplitude nor the b-wave amplitude differed significantly between the two groups ($n = 6$ animals, paired eyes). These findings indicate that no detectable impairment of retinal electrophysiological function was observed at the assessed time point under the tested conditions, further supporting the ocular tolerability of Best1-SOCS3 administration. To further evaluate whether RPE-restricted SOCS3 expression affected RPE proliferation or phenotype maintenance, we examined the proliferation markers Ki67 and PCNA, together with the RPE phenotypic marker RPE65, at 1 month after AAV-Best1-SOCS3 administration. Best1-SOCS3 treated eyes showed no obvious increase in Ki67 or PCNA positive signals in the RPE region compared with normal controls (Fig. S12B and Fig. S12C). RPE65 expression was also preserved after Best1-SOCS3 administration (Fig. S12D). Together with the ERG findings showing no obvious reduction in retinal responses, these results provide initial evidence against detectable RPE overgrowth, overt loss of RPE phenotypic marker expression, or obvious retinal functional impairment at the evaluated 1-month time point.

We next assessed potential neurological or behavioral toxicity using a visual cliff test (Fig. 6D). Heatmap recordings of mouse trajectories revealed comparable exploration patterns between the two groups (Fig. 6E). Quantitative analysis of the cumulative time spent in the safe zone indicated no detectable impairment in this visual behavior assay in the Best1-SOCS3 treated mice (Fig. 6F).

Finally, systemic toxicity was evaluated through hematological and histological analyses. Complete blood count revealed that red blood cells (RBC), white blood cells (WBC), platelets (PLT), and hemoglobin (Hb) levels were all within normal reference ranges (Fig. 6G). Assessment of liver and kidney function markers, including alanine aminotransferase (ALT), aspartate aminotransferase (AST), blood urea nitrogen (BUN), and lactate dehydrogenase (LDH), showed no significant elevation, indicating the absence of hepatotoxicity or nephrotoxicity (Fig. 6H). Consistent with these biochemical findings, histological examination (H&E staining) of major organs—heart, liver, spleen, lung, and kidney—displayed no obvious histopathological abnormalities (Fig. 6I). To further assess AAV-associated immune responses and systemic inflammatory status, we evaluated serum neutralizing activity against the AAV capsid and inflammatory cytokine levels after suprachoroidal Best1-SOCS3 administration. Detectable serum neutralizing activity was observed at 2 weeks and 1 month after injection, indicating a measurable humoral response to AAV delivery (Fig. S13A, B). However, at 1 month after administration, CD45 immunostaining showed no obvious inflammatory cell infiltration in Best1-SOCS3 treated eyes (Fig. S13C). Serum IL-1β, IL-6, IFN-γ, and TNF-α levels were also not significantly elevated compared with normal controls (Fig. S13D). These findings suggest that the detectable anti-AAV neutralizing activity was not accompanied by overt ocular inflammatory infiltration or systemic cytokine activation at the tested time point.

3. Discussion

This study establishes a dual-restricted ocular AAV platform for localized and cell-restricted therapeutic gene expression in the RPE. By combining suprachoroidal anatomical targeting with Best1 promoter-

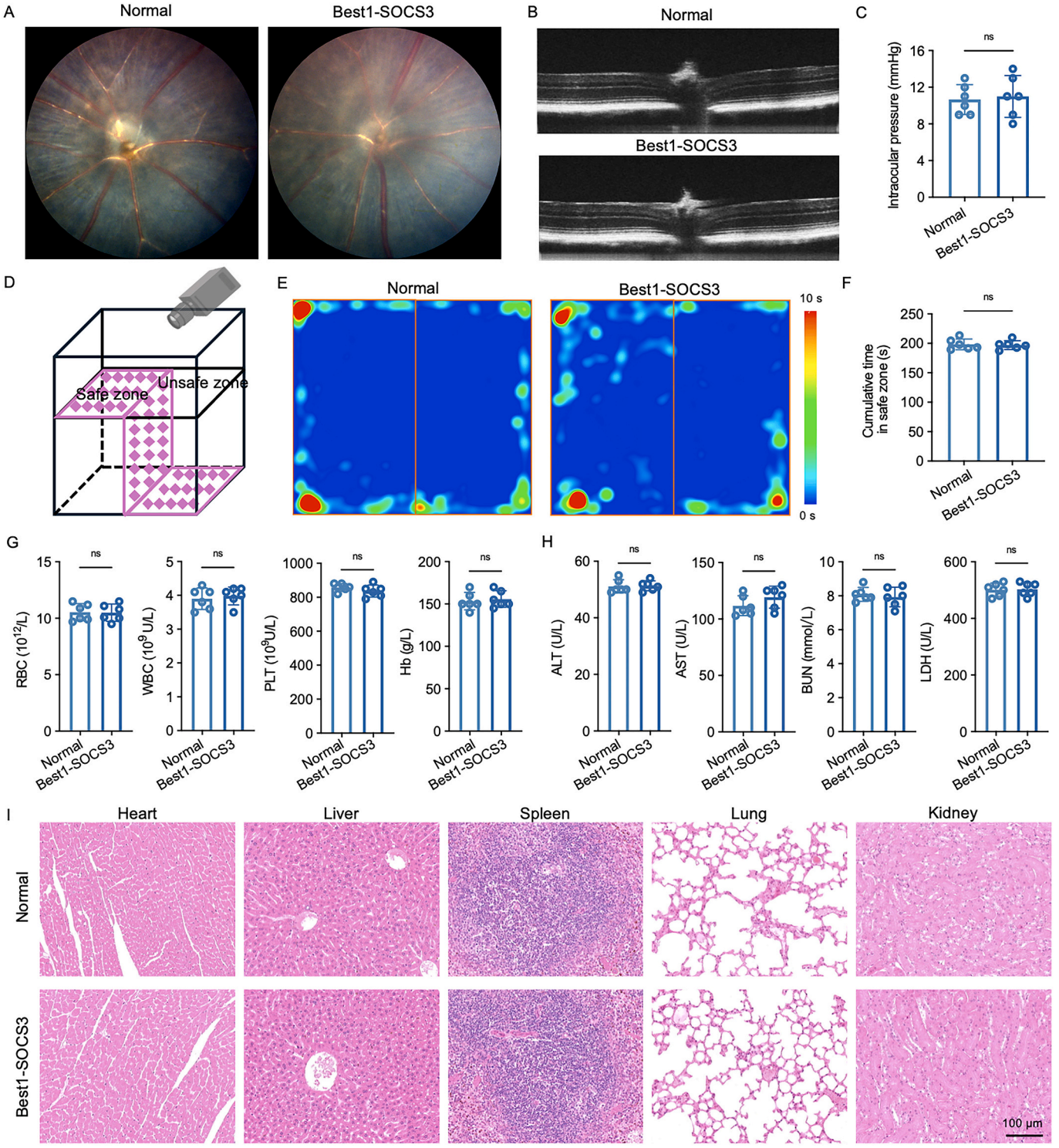

Fig. 6. Suprachoroidal AAV-Best1-SOCS3 exhibits a favorable biosafety profile.

(A, B) Ocular safety assessment. Representative fundus images (A) and OCT scan images (B) of mouse eyes 1-month post-injection, showing normal retinal morphology.

(C) IOP measurements indicating no significant difference between Normal and Best1-SOCS3 groups. ($n = 6$ biologically independent samples).

(D) Schematic illustration of the visual cliff test used to evaluate visual function and depth perception.

(E) Representative motion heatmaps showing the time spent in different zones. Red indicates areas of high occupancy.

(F) Statistical analysis of the time spent in the safe zone (shallow side), indicating intact visual function. ($n = 6$ biologically independent samples).

(G) Hematological analysis of whole blood, including RBC, WBC, PLT, and Hb counts. ($n = 6$ biologically independent samples).

(H) Serum biochemical analysis for liver (ALT, AST), kidney (BUN), and general tissue (LDH) function markers. ($n = 6$ biologically independent samples).

(I) Representative H&E staining of major organs (heart, liver, spleen, lung, kidney). All images share the same scale bars.

In the figure panels and quantitative plots, "Best1-SOCS3" denotes the group treated with AAV-Best1-SOCS3-3flag. Data in C, F, G and H are presented as mean ± SD and were compared *via* two tailed unpaired Student's *t*-test. ns, not significant. (For interpretation of the references to colour in this figure legend, the reader is referred to the web version of this article.)

mediated transcriptional restriction, AAV-Best1-SOCS3 achieved efficient RPE access, reduced ectopic expression in the neural retina, maintained ocular-localized expression for at least six months, and showed favorable ocular and systemic tolerability. These findings support layered control of both vector distribution and transgene expression as a strategy to improve the therapeutic index of posterior-segment gene therapy.

Efficient and safe RPE delivery remains challenging. Intravitreal administration is clinically convenient but has limited access to the outer retina because of the inner limiting membrane [28]. Subretinal injection provides highly efficient RPE and photoreceptor transduction but requires transretinal access and controlled formation of a subretinal bleb. This procedural distinction may be relevant to early-to-intermediate dAMD, in which viable RPE and photoreceptors remain therapeutic targets but the RPE-photoreceptor interface is already exposed to oxidative-inflammatory stress. Minimizing additional retinal penetration and mechanical manipulation may therefore be desirable. Suprachoroidal administration accesses the choroid-RPE interface through a transscleral route without deliberate neural-retinal penetration or separation and may offer a complementary, potentially less invasive approach, although suprachoroidal AAV delivery remains investigational.

Previous studies established the feasibility of suprachoroidal AAV delivery and BEST1/VMD2-based RPE-selective promoters [29,30]. Suprachoroidal administration improves vector access to the choroid-RPE interface but does not ensure RPE-specific expression, whereas an RPE-selective promoter restricts transcription without controlling vector distribution. Their combination therefore provides complementary anatomical and transcriptional control. In this study, suprachoroidal delivery enriched vector exposure toward the choroid-RPE interface, while Best1 further reduced neural retinal off-target expression compared with CMV under the same route and dose. Nevertheless, this restriction remains relative and may be influenced by vector dose, capsid properties, spatial distribution, and RPE pathological state.

Cell-restricted expression is particularly relevant for SOCS3 because STAT3 signaling has context-dependent functions across retinal cell types. Pathological STAT3 activation contributes to inflammatory RPE injury, whereas STAT3-related signaling may support neuronal stress responses and neuroprotection [31–33]. Ubiquitous SOCS3 overexpression could therefore suppress beneficial signaling in the neural retina. Restricting expression to the RPE may reduce this risk while preserving therapeutic activity at the intended site. Consistently, sustained Best1-driven SOCS3 expression was not associated with retinal thinning, structural disruption, functional impairment, behavioral abnormalities, or systemic organ toxicity under the tested conditions. The apparent tolerance of RPE-restricted SOCS3 expression may partly reflect the ability of RPE cells to maintain survival through alternative pathways, including PI3K/Akt and MAPK/ERK signaling [34,35]. More broadly, this dual-restricted design is conceptually aligned with biomaterial-assisted exosome and stimulus-responsive nanoparticle platforms that enhance local retention, preserve cargo activity, and reduce nonspecific exposure within pathological microenvironments [36,37]. In our platform, analogous spatial and cellular control is achieved through the combination of suprachoroidal targeting and Best1-mediated transcriptional restriction.

SOCS3 was selected because transcriptomic profiling and human dataset validation implicated SOCS3 deficiency and STAT3 hyperactivation in dAMD-related pathology. Oxidative stress and inflammation form a mutually reinforcing cycle in dAMD [38], whereas indiscriminate suppression of basal ROS may disrupt essential RPE functions, including outer-segment phagocytosis and cellular homeostasis [39]. Restoring SOCS3 instead reinforces an endogenous negative-feedback checkpoint upstream of this cycle. SOCS3 does not directly target STAT3 as a ligand-receptor or enzyme-substrate pair; rather, it limits excessive JAK-STAT signaling and thereby restrains STAT3 activation. In oxidatively stressed RPE cells, SOCS3 restoration reduced STAT3 activation, inflammatory cytokine production, ROS accumulation, mitochondrial disruption, barrier impairment, and cell death. In the $NaIO_3$-induced dAMD-like model, RPE-localized SOCS3 restoration similarly attenuated STAT3 hyperactivation, microglial/macrophage activation, inflammatory cytokine release, oxidative stress, mitochondrial injury, and apoptosis, with preservation of outer-retinal architecture. These findings suggest that restoring this endogenous checkpoint can interrupt the self-amplifying inflammatory-oxidative cycle.

Loss-of-function and rescue experiments strengthened this mechanistic interpretation. SOCS3 knockdown increased p-STAT3, ROS accumulation, mitochondrial disruption, ZO-1 loss, and cell death, whereas pharmacological STAT3 inhibition with Stattic partially rescued these abnormalities. The partial rescue achieved by Stattic indicates that excessive STAT3 activation contributes substantially to SOCS3-deficiency-associated RPE injury but does not fully account for the observed phenotype. Consistent with this interpretation, our transcriptomic analysis identified enrichment of NF-κB signaling, IL-17 signaling, and apoptosis-related pathways in addition to JAK-STAT activation. These pathways may operate in parallel with, or converge downstream of, oxidative stress to sustain inflammatory cytokine production, mitochondrial dysfunction, epithelial barrier disruption, and cell death. Moreover, ROS accumulation and mitochondrial injury can form self-amplifying cellular stress circuits that may persist even when STAT3 signaling is partially suppressed. Thus, the SOCS3-STAT3 axis should be regarded as an important amplifying node rather than the sole pathogenic pathway underlying oxidative-inflammatory RPE degeneration. Future studies combining SOCS3-STAT3 modulation with genetic or pharmacological inhibition of NF-κB-, IL-17-, apoptosis-, or redox/mitochondrial-related pathways will be required to define their relative contributions and evaluate potential combination strategies.

Durability and safety are essential for chronic retinal disease. Reporter imaging demonstrated ocular-localized expression for at least six months after a single suprachoroidal administration, with minimal systemic biodistribution. This durability may reduce the treatment burden associated with repeated intraocular administration. Fundus imaging, OCT, IOP, quantitative ERG, behavioral assessment, hematology, serum biochemistry, and major-organ histology revealed no overt toxicity under the tested conditions. Ki67, PCNA, RPE65, and ERG assessments provided initial evidence against abnormal RPE proliferation, overt loss of RPE phenotype, or obvious retinal dysfunction. However, these findings do not constitute a complete evaluation of long-term RPE homeostasis, and future studies should examine barrier integrity, phagocytic activity, visual-cycle function, and metabolic stability after sustained SOCS3 expression.

Immune safety also warrants continued evaluation. Neutralizing antibody and cytokine analyses showed detectable anti-AAV neutralizing activity but no overt ocular CD45-positive inflammatory infiltration or systemic cytokine elevation at the evaluated time point. Capsid-specific cellular immunity, tissue-resident responses, very long-term immune homeostasis, and repeat-dosing feasibility were not fully assessed. Because neutralizing activity may limit re-administration with the same capsid, future studies should examine alternative capsids, optimized dosing intervals, or appropriate immune-management strategies.

Several limitations should be considered. First, the experimental models used in this study do not fully recapitulate the chronic and multifactorial nature of human dAMD [25,40]. The $NaIO_3$ mouse model primarily reflects acute oxidative RPE injury with dAMD-like features, whereas the prolonged $NaIO_3$-treated ARPE-19 model provides complementary evidence under sustained oxidative stress but lacks the multicellular and aging-associated retinal microenvironment [41]. Therefore, these models should be regarded as complementary proof-of-concept systems. Further validation in chronic, aging-associated, or multifactorial animal models, followed by non-human primate studies, will be required to evaluate translational delivery, durability, immunogenicity, and long-term safety. Second, the timing of AAV-Best1-

SOCS3 administration remains an important translational consideration. Because AAV-mediated expression requires time to reach therapeutic levels, the prophylactic *in vivo* design should be interpreted as an early-intervention or disease-modifying proof of concept rather than an immediate rescue therapy for advanced dAMD. The strategy may be most relevant to early-to-intermediate disease, when stressed but viable RPE cells remain available for transduction, whereas benefit may be reduced in advanced geographic atrophy with extensive RPE loss. Third, Best1 activity may decline when chronic oxidative-inflammatory stress induces RPE dedifferentiation. Although Best1-driven expression remained detectable after acute $NaIO_3$ injury, equivalent promoter activity in advanced AMD cannot be assumed, and reduced activity could limit SOCS3 expression in viable RPE cells with a greater pathological burden. Future optimization could involve the development of RPE-selective, stress-amplified hybrid promoters. The feasibility of combining a cell-selective promoter with a pathological stimulus-responsive regulatory module has been demonstrated in retinal gene therapy [42]. Based on this precedent, oxidative stress-responsive elements, such as NRF2-responsive antioxidant response elements, could be evaluated together with compact RPE-selective regulatory elements to enhance SOCS3 expression under pathological stress while preserving RPE restriction. Such candidate promoters would require systematic evaluation of inducibility, cellular specificity, off-target activation, and long-term stability.

Finally, dose-ranging analysis showed that RPE 3flag expression increased from 5×10^9 to 2×10^{10} vg/eye but did not increase further at 4×10^{10} vg/eye, indicating an expression plateau near 2×10^{10} vg/eye. Together with the ocular and systemic safety data obtained at this dose, these findings support 2×10^{10} vg/eye as the lowest tested dose achieving near-maximal RPE transgene expression without overt toxicity under the tested conditions. Broader dose-ranging studies incorporating parallel efficacy and longer-term safety assessments will be needed for further translational optimization.

In summary, suprachoroidal delivery combined with Best1-mediated transcriptional restriction enabled localized, durable, and RPE-restricted AAV expression. Using SOCS3 as the therapeutic cargo, this platform attenuated STAT3-associated oxidative-inflammatory degeneration while limiting neural-retinal and systemic exposure. These findings support further preclinical development of AAV-Best1-SOCS3 as a controlled ocular gene therapy strategy for dAMD.

4. Materials and methods

4.1. Age-related macular degeneration model establishment

Male C57BL/6J mice (6–8 weeks old) were used in this study. All animal experiments were approved by the Institutional Animal Care and Use Committee (IACUC) and conducted in accordance with the Association for Research in Vision and Ophthalmology (ARVO) Statement for the Use of Animals in Ophthalmic and Vision Research. To establish the $NaIO_3$-induced dAMD-like model, mice received a single intraperitoneal injection of sodium iodate ($NaIO_3$, 35 mg/kg) dissolved in sterile saline. The control group received an equivalent volume of sterile saline vehicle.

4.2. RNA extraction, library preparation, and sequencing

Total RNA was extracted from RPE/choroid complexes of normal and $NaIO_3$-treated mice using TRIzol reagent according to the manufacturer's protocol. RNA concentration, purity, and integrity were assessed using a NanoDrop spectrophotometer before library preparation. Sequencing libraries were generated according to the following steps. Firstly, mRNA was purified from total RNA using poly-T oligo-attached magnetic beads. Fragmentation was carried out using divalent cations under elevated temperature in an Illumina proprietary fragmentation buffer. First strand cDNA was synthesized using random oligonucleotides and Super Script II. Second strand cDNA synthesis was subsequently performed using DNA Polymerase I and RNase H. Remaining overhangs were converted into blunt ends *via* exonuclease/polymerase activities and the enzymes were removed. After adenylation of the 3′ ends of the DNA fragments, Illumina PE adapter oligonucleotides were ligated to prepare for hybridization. To select cDNA fragments of the preferred 400–500 bp in length, the library fragments were purified using the AMPure XP system (Beckman Coulter, Beverly, CA, USA). DNA fragments with ligated adaptor molecules on both ends were selectively enriched using Illumina PCR Primer Cocktail in a 15-cycle PCR reaction. Products were purified (AMPure XP system) and quantified using the Agilent high sensitivity DNA assay on a Bioanalyzer 2100 system (Agilent). The sequencing library was then sequenced on NovaSeq 6000 platform (Illumina) Shanghai Personal Biotechnology Co. Ltd. Differential gene expression analysis was performed by DESeq2 software between the two groups. The genes with the parameter of false discovery rate below 0.05 and absolute fold change ≥ 2 were considered differentially expressed genes.

4.3. Immunofluorescence staining

4.3.1. Retina tissue immunofluorescence staining

For histological analysis, enucleated eyes were fixed in 4% paraformaldehyde (PFA) for 24 h and then embedded in OCT compound. The frozen eyeballs were cut into 6–7 μm tissue sections using a frozen microtome (Leica) and imaged using the CLSM (Nikon A1R). The primary antibodies used for staining were 3flag (abcam, ab205606), SOCS3 (immunoway, YM9212), p-STAT3 (abcam, ab267373), IBA1 (abcam, ab178846), TOM20 (abcam, ab186735), and RPE65 (abcam, ab231782). Nuclei were counterstained with DAPI.

4.3.2. Cell immunofluorescence staining

ARPE-19 cells were cultured on glass coverslips and fixed with 4% paraformaldehyde (PFA) for 15 min at room temperature, permeabilized with 0.1% Triton X-100 in PBS for 10 min, and blocked with 5% BSA for 1 h. The cells were then incubated overnight at 4 °C with primary antibodies against 3flag (abcam, ab205606), SOCS3 (immunoway, YM9212), p-STAT3 (abcam, ab267373), TOM20 (abcam, ab186735), and ZO-1 (abcam, ab221547) and RPE65 (abcam, ab231782). Nuclei were counterstained with DAPI. The images were observed under CLSM (Nikon A1R).

4.4. Enzyme-linked immunosorbent assay (ELISA)

4.4.1. RPE/choroid tissues ELISA

RPE/choroid tissues were harvested and homogenized in cold PBS containing RIPA lysis buffer with 1% protease inhibitor mixture and 1% phosphatase inhibitor mixture. The supernatants were collected after centrifugation. The concentrations of inflammatory cytokines, including IL-1β, IL-6, TNF-α, and IFN-γ, were quantified using commercial ELISA kits (Solarbio) following the manufacturer's protocols. Absorbance was measured at 450 nm using a microplate reader. The ELISA kits for cytokines were purchased from Solarbio.

4.4.2. Cell culture supernatants ELISA

The levels of inflammatory cytokines, including IL-1β, IL-6, TNF-α, and IFN-γ, in the cell culture supernatants were quantified using commercial ELISA kits (Solarbio) according to the manufacturer's instructions. The optical density (OD) was measured at 450 nm using a microplate reader.

4.5. AAV vector design and experimental purposes

A schematic summary of the AAV constructs is provided in Fig. S14. All vectors were packaged in the AAV8 capsid. AAV-CMV-SOCS3-3flag and AAV-Best1-SOCS3-3flag were used for *in vitro* mechanistic studies

and *in vivo* efficacy/safety or dose–expression analyses, respectively. In AAV-CMV-SOCS3-EGFP, AAV-Best1-SOCS3-EGFP, and AAV-Best1-SOCS3-Luciferase, SOCS3 and the reporter were encoded in the same cassette and separated by a T2A peptide. AAV-CMV-SOCS3-EGFP and AAV-Best1-SOCS3-EGFP were used for route- and promoter-dependent expression analyses, whereas AAV-Best1-SOCS3-Luciferase was used for biodistribution and longitudinal expression monitoring. AAV-Best1-Null served as the empty-vector control.

For clarity, full construct names are used when referring to the vectors themselves, whereas shortened labels are reserved for treatment groups in figure panels and quantitative plots. "CMV-SOCS3" denotes treatment with AAV-CMV-SOCS3-3flag; "CMV-SOCS3-EGFP" and "Best1-SOCS3-EGFP" denote treatment with AAV-CMV-SOCS3-EGFP and AAV-Best1-SOCS3-EGFP, respectively; "Best1-SOCS3" denotes treatment with the therapeutic vector AAV-Best1-SOCS3-3flag; and "Best1-Null" denotes treatment with AAV-Best1-Null. Each shortened label refers to one uniquely defined construct, and distinct constructs are not represented by the same group label.

4.6. Cell culture and AAV transduction

ARPE-19 were cultured in DMEM/F12 medium supplemented with 10% fetal bovine serum (FBS) and 1% penicillin/streptomycin at 37 °C in a 5% CO_2 incubator.

To verify the transduction efficiency *in vitro*, ARPE-19 cells were seeded into 12-well plates. Upon reaching 70% confluence, cells were transduced with the AAV vectors: CMV-SOCS3-3flag at a multiplicity of infection (MOI) of 10^5. The cells were incubated for 48 h to allow for transgene expression.

4.7. Cell culture and in vitro model establishment

ARPE-19 were cultured in DMEM/F12 medium supplemented with 10% fetal bovine serum (FBS) and 1% penicillin/streptomycin at 37 °C in a humidified atmosphere containing 5% CO_2. To mimic the oxidative stress environment of dAMD, cells were stimulated with hydrogen peroxide (H_2O_2, 300 μM) for 6 h.

4.8. Gene expression and experimental grouping in vitro

For the therapeutic evaluation, ARPE-19 cells were randomly divided into three groups: Normal, PBS (H_2O_2 + PBS), and CMV-SOCS3 (H_2O_2 + AAV-CMV-SOCS3). Cells in the treatment group were transduced with the AAV-CMV-SOCS3-3flag vector, while the control group was treated with an equivalent volume of PBS. The pre-treatment was performed for 48 h to ensure adequate expression of SOCS3 prior to the 6 h H_2O_2 stimulation.

4.9. In vitro ROS detection

The cells were washed three times with PBS and incubated with a DCFH-DA probe (Solarbio) for 30 min while cells were protected from light. The level of ROS within cells was observed under CLSM (Nikon A1R).

4.10. Live/dead cell assay

Cell viability was assessed using a Calcein-AM/Propidium Iodide (PI) Double Staining Kit (Beyotime). Briefly, cells were washed and incubated with the assay solution containing Calcein-AM (staining live cells green) and PI (staining dead cells red) for 30 min at 37 °C. The images were observed under CLSM (Nikon A1R).

4.11. Mitochondrial membrane potential assessment

Mitochondrial membrane potential in ARPE-19 cells was assessed using a JC-1 mitochondrial membrane potential assay kit (Solarbio, Beijing, China; Cat. No. M8650) according to the manufacturer's instructions. ARPE-19 cells were seeded on glass coverslips and divided into three groups: Normal, PBS, and CMV-SOCS3. Cells in the CMV-SOCS3 group were transduced with AAV-CMV-SOCS3 for 48 h, while cells in the PBS group received an equivalent volume of PBS. Cells in the PBS and CMV-SOCS3 groups were then exposed to H_2O_2 for 6 h to induce oxidative injury. After treatment, cells were washed with PBS and incubated with JC-1 working solution at 37 °C for 20 min in the dark. Cells were then washed with JC-1 staining buffer and immediately imaged by confocal laser scanning microscopy. JC-1 monomers were detected as green fluorescence, whereas JC-1 aggregates were detected as red fluorescence.

4.12. Prolonged $NaIO_3$-induced oxidative RPE injury model in ARPE-19 cells

ARPE-19 cells were seeded into culture plates or onto coverslips on Day −1 and allowed to adhere overnight. From Day 0 to Day 5, cells were continuously exposed to 5 mM $NaIO_3$ in complete culture medium to induce sustained oxidative RPE stress. To model intervention after injury initiation, PBS or AAV-CMV-SOCS3-3flag was administered on Day 2, while $NaIO_3$ exposure was continued until Day 5. Cells and culture supernatants were then collected for subsequent analyses, including 3flag and p-STAT3 immunofluorescence staining, ROS detection, TOM20 and ZO-1 immunofluorescence staining, Calcein AM/PI cell viability/death assessment, and ELISA analysis of inflammatory cytokines.

4.13. siRNA-mediated SOCS3 knockdown and Stattic rescue in ARPE-19 cells

For SOCS3 loss-of-function and STAT3 inhibition rescue experiments, ARPE-19 cells were transfected with siNC or siSOCS3 at a final concentration of 50 nM using Lipofectamine RNAiMAX, (Thermo Fisher, Cat. No. 13778150) according to the manufacturer's instructions. After 48 h of transfection, cells were exposed to 300 μM H_2O_2 for 6 h where indicated. In the rescue group, Stattic (Selleckchem, Cat. No. S7024) was added at 10 μM together with H_2O_2. The experimental groups included siNC, siSOCS3, H_2O_2 + siNC, H_2O_2 + siSOCS3, and H_2O_2 + siSOCS3 + Stattic. Cells were then collected for qPCR analysis, p-STAT3 immunofluorescence staining, ROS detection, TOM20 and ZO-1 immunofluorescence staining, and Calcein AM/PI cell viability assessment.

4.14. Electron microscopy of mitochondria

4.14.1. Cell electron microscopy

ARPE-19 cells were harvested by centrifugation, and the resulting pellets were immediately fixed with an electron microscopy fixative at 4 °C for 2–4 h. The above samples were tested by Wuhan Servicebio Technology CO., LTD. The ultrastructure of mitochondria in retina was examined by electron microscopy.

4.14.2. Retinal tissues electron microscopy

Eyeballs were excised and dissected to obtain the retina. The tissues were immediately immersed in a 2.5% glutaraldehyde solution at 4 °C. The entire process was limited to less than 2 min. The above samples were tested by Wuhan Servicebio Technology CO., LTD. The ultrastructure of mitochondria in retina was examined by electron microscopy.

4.15. Dose-expression analysis of AAV-Best1-SOCS3 following suprachoroidal administration

To characterize the dose–expression relationship and determine whether RPE transgene expression approached saturation, mice

received suprachoroidal administration of AAV-Best1-SOCS3-3flag at four doses: 5×10^9, 1×10^{10}, 2×10^{10}, and 4×10^{10} vg/eye ($n = 6$ biologically independent animals per group). All vectors were packaged with the AAV8 capsid and administered in the same injection volume of 2 μL per eye using a microneedle, with the vector concentration adjusted according to the designated dose.

At 1 month after administration, eyes were collected and retinal sections were prepared for immunofluorescence analysis. Transgene-derived SOCS3 expression was detected using an anti-flag antibody (Abcam, ab205606), and nuclei were counterstained with DAPI. Images from all dose groups were acquired under identical imaging conditions. The 3flag fluorescence signal within the RPE layer was quantified as integrated fluorescence density.

4.16. Suprachoroidal gene delivery and $NaIO_3$-induced dAMD-like model induction

The experimental timeline is illustrated. A microneedle (Hamilton) was used to perform suprachoroidal injection. All AAV vectors used in this study were packaged with the AAV8 capsid. The viral genome titer was adjusted to 1.0×10^{13} vg/mL, as determined by qPCR. For suprachoroidal administration, each mouse eye received 2 μL of AAV solution, corresponding to a total dose of 2.0×10^{10} vg/eye. Reporter vectors and therapeutic AAV-Best1-SOCS3-3flag vectors were administered at equivalent viral genome doses. Mice received 2 μL of AAV-Best1-SOCS3-3flag or PBS vehicle into the suprachoroidal space. One-month post-injection, $NaIO_3$-induced dAMD-like model was induced by a single intraperitoneal injection of $NaIO_3$ dissolved in sterile saline. The "Normal" group received an equivalent volume of saline. Mice were sacrificed for analysis one week after $NaIO_3$ administration.

4.17. Subretinal injection experiment

For the subretinal route-comparison experiment, mice received subretinal injection of AAV-CMV-SOCS3-EGFP to evaluate anatomical AAV access to the outer retina/RPE region. The CMV-driven reporter vector was used in this experiment to visualize the anatomical distribution of AAV-mediated transgene expression after subretinal delivery. AAV-CMV-SOCS3-EGFP was administered at the same viral genome dose used for the corresponding route-comparison experiments. After injection, successful subretinal delivery was confirmed by direct visualization of localized bleb formation during the procedure. Retinal tissues were collected at the same time point used for the intravitreal and suprachoroidal route-comparison experiments and processed for EGFP immunofluorescence analysis.

4.18. Gene expression in vivo

To verify transgene expression and pathway inhibition, retinal protein levels were assessed. Immunofluorescence staining was performed using antibodies against 3flag (abcam, ab205606).

4.19. Color fundus photography

Color fundus photography was performed using a retinal imaging system (Optoprobe Science). The fixed and anesthetized mice were placed on the lifting table. The pupils were routinely administered with compound tropicamide eye drops and proparacaine hydrochloride eye drops for dilation and epidermal anesthesia, respectively. Carbomer eye drops were applied to the cornea so that the cornea was in contact with the microscope lens of the fundus imaging system. Afterwards, the focal length of the test bed and lens was adjusted, and pictures were taken.

4.20. OCT

Retinal scans of mouse eyes were acquired by OCT imaging using an ultramicro ophthalmol imaging system (Optoprobe Science, United Kingdom).

4.21. H&E staining

For histological analysis, eyes were enucleated, fixed in 4% paraformaldehyde (PFA) for 24 h, and embedded in paraffin. Sagittal sections (5 μm) passing through the optic nerve head were collected and stained with hematoxylin and eosin (H&E).

4.22. Morphometric analysis

To quantify the protective effect of the gene therapy, morphometric analysis was performed on H&E-stained sections. The thickness of the ONL and INL was measured using ImageJ software (NIH, USA). Additionally, the number of nuclei in the ONL and INL columns was counted in a masked fashion to assess photoreceptor and neuronal survival.

4.23. Measurement of retinal ROS

To evaluate oxidative stress levels *in situ*, the production of ROS in the retina was detected using Dihydroethidium (DHE) staining. Freshly prepared frozen retinal sections were incubated with the ROS staining solution in a humidified chamber at 37 °C for 30 min in the dark. Sections were washed with PBS, and nuclei were stained with DAPI. The fluorescence intensity of ROS (red) was visualized immediately using a fluorescence microscope.

4.24. TUNEL apoptosis assay

Apoptosis in retinal tissues was assessed using a Terminal Deoxynucleotidyl Transferase dUTP Nick End Labeling (TUNEL) assay kit, according to the manufacturer's instructions. Briefly, retinal sections were permeabilized and incubated with the TUNEL reaction mixture containing rTdT enzyme and nucleotide mix for 1 h at 37 °C. Green fluorescence indicated apoptotic cells. Nuclei were stained with DAPI.

4.25. Biodistribution and organ expression profile

To evaluate the tissue specificity and potential systemic leakage of the suprachoroidally delivered AAV vector, biodistribution analysis was performed. Mice received a suprachoroidal injection of AAV-Best1-SOCS3-Luciferase as described above. At 1 month post-injection, mice were sacrificed, and major organs, including the eye, heart, liver, spleen, lung, kidney, and brain, were harvested immediately. The organs were arranged on a black plate and imaged *ex vivo* using IVIS Spectrum imaging system (PerkinElmer). The bioluminescence signal intensity was quantified as Total Flux (photons/second, p/s) using Living Image 4.5 software.

4.26. Quantitative PCR analysis of AAV biodistribution

Genomic DNA was extracted from the injected eye and major organs using a genomic DNA extraction kit according to the manufacturer's instructions. AAV vector abundance was quantified by qPCR using primers targeting the WPRE sequence. β-actin was used as an internal reference to normalize genomic DNA input.

4.27. Long-term in vivo bioluminescence imaging

To monitor the stability and duration of transgene expression, longitudinal *in vivo* imaging was conducted at 1, 2, 3, 4, 5, and 6 months post-injection of AAV-Best1-SOCS3-Luciferase. Mice were anesthetized with isoflurane (2% for induction, 1.5% for maintenance). D-Luciferin 150 mg/kg dissolved in sterile PBS was administered *via* intraperitoneal injection. Ten minutes after substrate injection, mice were placed in the

dark chamber of the IVIS Spectrum imaging system (PerkinElmer).

For quantitative analysis, a fixed Region of Interest (ROI) was drawn around the eye, and the Average Radiance (p/s/cm^2/sr) was calculated to represent the transgene expression level. Data were normalized to the baseline or presented as absolute values to depict the expression kinetics over time.

4.28. Visual cliff

The visual cliff test was conducted to evaluate visual function based on previous established methods [43]. The apparatus consisted of two plastic boxes, with the first box measuring 50 cm by 40 cm by 50 cm and featuring a checkerboard pattern of black and white squares, each 2 cm by 2 cm, on half of its top and bottom. The second box, placed on top, had a transparent bottom and black side walls, creating two sections: a "safe zone" above the checkerboard and an "unsafe zone," where the cliff formed by the transparent floor over the checkerboard base. Mice were placed in the safe zone and allowed to explore for 5 min. Their movements were captured, and the time spent in each zone was evaluated using ANY-maze software (Stoelting Co., Wood Dale, USA).

4.29. ERG

Before ERG recording, mice were dark-adapted for 12 h and prepared under dim red illumination. After anesthesia and pupil dilation, the cornea was topically anesthetized. The recording electrode was placed on the cornea, the reference electrode was placed on the cheek, and a subcutaneous electrode inserted into the tail served as the ground. Under scotopic conditions, a 3.0 cd·s·m-2 flash stimulus was delivered for 5 ms, with an inter-stimulus interval of 15 s to allow retinal recovery. Each flash stimulus was repeated at least three times. The recorded waveforms were exported and analyzed using a visual electrophysiology system (Optoprobe Science).

4.30. Safety assessment in vivo

The *in vivo* safety assessment was performed 1 month after the injection of AAV-Best1-SOCS3-3flag. To assess ocular safety, intraocular pressure was measured using an iCare tonometer (TONOLAB); color fundus photography was performed using a retinal imaging system (Optoprobe Science); and OCT was performed with an ultramicro ophthalmol imaging system (Optoprobe Science, UK). For H&E staining, paraffin-embedded harvested heart, liver, spleen, lung, and kidney were sectioned into 10 μm tissue sections and subsequently subjected to H&E staining. Whole blood was collected for blood routine tests, which included white blood cell (WBC), red blood cell (RBC), platelet (PLT), and hemoglobin levels (Hb). Serum levels of alanine aminotransferase (ALT), aspartate aminotransferase (AST), blood urea nitrogen (BUN), and lactate dehydrogenase (LDH) were analyzed using an automated analyzer.

4.31. AAV neutralizing antibody assay

To assess AAV-associated humoral immune responses, serum neutralizing activity against the AAV capsid was measured using an AAV-CMV-Luc transduction inhibition assay. Serum samples were collected at 2 weeks and 1 month after suprachoroidal AAV-Best1-SOCS3-3flag administration. Serial serum dilutions ranging from 1:2 to 1:1024 were incubated with a fixed amount of AAV-CMV-Luc reporter vector carrying the same capsid as the therapeutic vector at 37 °C for 1 h. The serum-AAV-CMV-Luc mixtures were then added to HEK293T cells seeded in 96-well plates. After 24 h, luciferase activity was measured using a luciferase assay system. Relative AAV-CMV-Luc transduction was calculated as the percentage of luciferase activity relative to the AAV-CMV-Luc-only control. Lower relative transduction indicated stronger neutralizing activity, and normal mouse serum was used as a negative control.

4.32. Statistical analysis

Statistical analyses were performed using GraphPad Prism 9. All graphs present mean ± S.D. unless otherwise specified. A two-tailed unpaired Student's *t*-test was used for comparisons between two independent groups, whereas a two-tailed paired Student's *t*-test was used for paired comparisons between contralateral eyes from the same animal. One-way analysis of variance (ANOVA) was used to compare multiple groups, with *post hoc* multiple-comparison tests applied as specified in the corresponding figure legends. P values <0.05 were considered statistically significant.

CRediT authorship contribution statement

Yiquan Zhang: Writing – original draft, Methodology, Formal analysis, Conceptualization. **Fuxiao Luan:** Data curation. **Jing Feng:** Writing – review & editing, Supervision, Data curation, Conceptualization. **Wenqiang Sun:** Writing – review & editing, Supervision, Methodology. **Yong Tao:** Writing – review & editing, Supervision, Conceptualization.

Ethics approval statement

The mouse experiments were approved by the IACUC of the Capital Medical University (AEEI-2026-124). All procedures were conducted in accordance with the ARVO Statement for the Use of Animals in Ophthalmic and Vision Research.

Author contributions

Yong Tao and Yiquan Zhang designed the research; Yiquan Zhang and Jing Feng performed the research and analyzed the data; Fuxiao Luan assisted with the establishment of mouse model; Yiquan Zhang wrote the paper, with feedback and support from Wenqiang Sun and Yong Tao. All authors have given approval to the final version of the manuscript.

Declaration of competing interest

The authors declare no conflict of interest.

Acknowledgements

This work was supported by the National Natural Science Foundation of China (82471081 to Y.T., 82302064 to W.S.), the National Key Research and Development Program of China (2025YFA1212700 to Y.T., 2023YFC2508504 to W.S.), the Beijing Hospitals Authority's Ascent Program (DFL20220301 to Y.T.), the Excellent Young Talent Innovation Project of Chinese Institutes for Medical Research (CX23YQA02 to Y.T.), and the Chinese Institutes for Medical Research (CX23YQ03 to Y.T.) and the Beijing Natural Science Foundation (7262167 to W.S.), Beijing Hospitals Authority Clinical Medicine Development of Special Funding Support (YGLX202508), Beijing Municipal Administration of Hospitals Incubating Program (PX20240303).

Appendix A. Supplementary data

Supplementary data to this article can be found online at https://doi.org/10.1016/j.jconrel.2026.115289.

Data availability

Materials and datasets used and/or analyzed during the current study are available from the corresponding author upon reasonable

request.

References

[1] P. Mitchell, G. Liew, B. Gopinath, T.Y. Wong, Age-related macular degeneration, Lancet 392 (2018) 1147–1159, https://doi.org/10.1016/S0140-6736(18)31550-2.

[2] M. Fleckenstein, T.D.L. Keenan, R.H. Guymer, U. Chakravarthy, S. Schmitz-Valckenberg, C.C. Klaver, W.T. Wong, E.Y. Chew, Age-related macular degeneration, Nat. Rev. Dis. Prim. 7 (2021) 31, https://doi.org/10.1038/s41572-021-00265-2.

[3] M. Fleckenstein, P. Mitchell, K.B. Freund, S. Sadda, F.G. Holz, C. Brittain, E. C. Henry, D. Ferrara, The progression of geographic atrophy secondary to age-related macular degeneration, Ophthalmology 125 (2018) 369–390, https://doi.org/10.1016/j.ophtha.2017.08.038.

[4] J.T. Handa, C. Bowes Rickman, A.D. Dick, M.B. Gorin, J.W. Miller, C.A. Toth, M. Ueffing, M. Zarbin, L.A. Farrer, A systems biology approach towards understanding and treating non-neovascular age-related macular degeneration, Nat. Commun. 10 (2019) 3347, https://doi.org/10.1038/s41467-019-11262-1.

[5] D. Dalkara, K.D. Kolstad, N. Caporale, M. Visel, R.R. Klimczak, D.V. Schaffer, J. G. Flannery, Inner limiting membrane barriers to AAV-mediated retinal transduction from the vitreous, Mol. Ther. 17 (2009) 2096–2102, https://doi.org/10.1038/mt.2009.181.

[6] D. L'Abbate, K. Prescott, B. Geraghty, V.R. Kearns, D.H.W. Steel, Biomechanical considerations for optimising subretinal injections, Surv. Ophthalmol. 69 (2024) 722–732, https://doi.org/10.1016/j.survophthal.2024.05.004.

[7] D.M. Wu, X. Ji, M.V. Ivanchenko, M. Chung, M. Piper, P. Rana, S.K. Wang, Y. Xue, E. West, S.R. Zhao, et al., Nrf2 overexpression rescues the RPE in mouse models of retinitis pigmentosa, JCI Insight 6 (2021) e145029, https://doi.org/10.1172/jci.insight.145029.

[8] X. Hu, J. Li, M. Fu, X. Zhao, W. Wang, The JAK/STAT signaling pathway: from bench to clinic, Signal. Transduct. Target Ther. 6 (2021) 402, https://doi.org/10.1038/s41392-021-00791-1.

[9] K. Jiang, K.L. Wright, P. Zhu, M.J. Szego, A.N. Bramall, W.W. Hauswirth, Q. Li, S. E. Egan, R.R. McInnes, STAT3 promotes survival of mutant photoreceptors in inherited photoreceptor degeneration models, Proc. Natl. Acad. Sci. USA 111 (2014), https://doi.org/10.1073/pnas.1411248112.

[10] Y. Wang, A. Rajala, B. Cao, M. Ranjo-Bishop, M.-P. Agbaga, C. Mao, R.V.S. Rajala, Cell-specific promoters enable lipid-based nanoparticles to deliver genes to specific cells of the retina *in vivo*, Theranostics 6 (2016) 1514–1527, https://doi.org/10.7150/thno.15230.

[11] J. Ambati, J.P. Atkinson, B.D. Gelfand, Immunology of age-related macular degeneration, Nat. Rev. Immunol. 13 (2013) 438–451, https://doi.org/10.1038/nri3459.

[12] U. Gupta, S. Ghosh, C.T. Wallace, P. Shang, Y. Xin, A.P. Nair, M. Yazdankhah, A. Strizhakova, M.A. Ross, H. Liu, et al., Increased LCN2 (lipocalin 2) in the RPE decreases autophagy and activates inflammasome-ferroptosis processes in a mouse model of dry AMD, Autophagy 19 (2023) 92–111, https://doi.org/10.1080/15548627.2022.2062887.

[13] S. Datta, M. Cano, K. Ebrahimi, L. Wang, J.T. Handa, The impact of oxidative stress and inflammation on RPE degeneration in non-neovascular AMD, Prog. Retin. Eye Res. 60 (2017) 201–218, https://doi.org/10.1016/j.preteyeres.2017.03.002.

[14] X. Guillonneau, C.M. Eandi, M. Paques, J.-A. Sahel, P. Sapieha, F. Sennlaub, On phagocytes and macular degeneration, Prog. Retin. Eye Res. 61 (2017) 98–128, https://doi.org/10.1016/j.preteyeres.2017.06.002.

[15] K. Kaarniranta, H. Uusitalo, J. Blasiak, S. Felszeghy, R. Kannan, A. Kauppinen, A. Salminen, D. Sinha, D. Ferrington, Mechanisms of mitochondrial dysfunction and their impact on age-related macular degeneration, Prog. Retin. Eye Res. 79 (2020) 100858, https://doi.org/10.1016/j.preteyeres.2020.100858.

[16] D.S.A. Simpson, P.L. Oliver, ROS generation in microglia: understanding oxidative stress and inflammation in neurodegenerative disease, Antioxidants (Basel, Switzerland) 9 (2020) 743, https://doi.org/10.3390/antiox9080743.

[17] H. Qin, J.A. Buckley, X. Li, Y. Liu, T.H. Fox, G.P. Meares, H. Yu, Z. Yan, A.S. Harms, Y. Li, et al., Inhibition of the JAK/STAT pathway protects against α-synuclein-induced neuroinflammation and dopaminergic neurodegeneration, J. Neurosci. 36 (2016) 5144–5159, https://doi.org/10.1523/JNEUROSCI.4658-15.2016.

[18] A. Yoshimura, T. Naka, M. Kubo, SOCS proteins, cytokine signalling and immune regulation, Nat. Rev. Immunol. 7 (2007) 454–465, https://doi.org/10.1038/nri2093.

[19] R. Nakamura, A. Sene, A. Santeford, A. Gdoura, S. Kubota, N. Zapata, R.S. Apte, IL10-driven STAT3 signalling in senescent macrophages promotes pathological eye angiogenesis, Nat. Commun. 6 (2015) 7847, https://doi.org/10.1038/ncomms8847.

[20] X. Chen, R. Sun, D. Yang, C. Jiang, Q. Liu, LINC00167 regulates RPE differentiation by targeting the miR-203a-3p/SOCS3 Axis, Mol. Ther. Nucleic Acids 19 (2020) 1015–1026, https://doi.org/10.1016/j.omtn.2019.12.040.

[21] T.A. Bailey, N. Kanuga, I.A. Romero, J. Greenwood, P.J. Luthert, M.E. Cheetham, Oxidative stress affects the junctional integrity of retinal pigment epithelial cells, Invest. Ophthalmol. Vis. Sci. 45 (2004) 675, https://doi.org/10.1167/iovs.03-0351.

[22] G.A. Ochakovski, K.U. Bartz-Schmidt, M.D. Fischer, Retinal gene therapy: surgical vector delivery in the translation to clinical trials, Front. Neurosci. 11 (2017), https://doi.org/10.3389/fnins.2017.00174.

[23] C. Irigoyen, A. Amenabar Alonso, J. Sanchez-Molina, M. Rodríguez-Hidalgo, A. Lara-López, J. Ruiz-Ederra, Subretinal injection techniques for retinal disease: a review, J. Clin. Med. 11 (2022) 4717, https://doi.org/10.3390/jcm11164717.

[24] Y.-S. Liu, J.-Q. Pan, X.-B. Pan, F.-S. Kong, J.-Q. Zhang, Z.-Y. Wei, Z.-H. Xu, J.-H. Rao, J.-H. Wang, J.-H. Chen, Comparative analysis of molecular landscape in mouse models and patients reveals conserved inflammation pathways in age-related macular degeneration, Invest. Ophthalmol. Vis. Sci. 65 (2024) 13, https://doi.org/10.1167/iovs.65.1.13.

[25] M.E. Pennesi, M. Neuringer, R.J. Courtney, Animal models of age related macular degeneration, Mol. Asp. Med. 33 (2012) 487–509, https://doi.org/10.1016/j.mam.2012.06.003.

[26] G. Chowers, M. Cohen, D. Marks-Ohana, S. Stika, A. Eijzenberg, E. Banin, A. Obolensky, Course of sodium iodate–induced retinal degeneration in albino and pigmented mice, Invest. Ophthalmol. Vis. Sci. 58 (2017) 2239, https://doi.org/10.1167/iovs.16-21255.

[27] M. Allocca, C. Mussolino, M. Garcia-Hoyos, D. Sanges, C. Iodice, M. Petrillo, L. H. Vandenberghe, J.M. Wilson, V. Marigo, E.M. Surace, et al., Novel adeno-associated virus serotypes efficiently transduce murine photoreceptors, J. Virol. 81 (2007) 11372–11380, https://doi.org/10.1128/JVI.01327-07.

[28] M.J. Patel, S. Sheth, J. Mar, N.Z. Gregori, J.D. Sengillo, Surgical approaches to retinal gene therapy: 2025 update, Bioengineering (Basel, Switzerland) 12 (2025) 1122, https://doi.org/10.3390/bioengineering12101122.

[29] K. Ding, J. Shen, Z. Hafiz, S.F. Hackett, R.L.E. Silva, M. Khan, V.E. Lorenc, D. Chen, R. Chadha, M. Zhang, et al., AAV8-vectored suprachoroidal gene transfer produces widespread ocular transgene expression, J. Clin. Invest. 129 (2019) 4901–4911, https://doi.org/10.1172/JCI129085.

[30] K.E. Guziewicz, B. Zangerl, A.M. Komáromy, S. Iwabe, V.A. Chiodo, S.L. Boye, W. W. Hauswirth, W.A. Beltran, G.D. Aguirre, Recombinant AAV-mediated BEST1 transfer to the retinal pigment epithelium: analysis of serotype-dependent retinal effects, PLoS One 8 (2013) e75666, https://doi.org/10.1371/journal.pone.0075666.

[31] M. Hellström, J. Muhling, E.M. Ehlert, J. Verhaagen, M.A. Pollett, Y. Hu, A. R. Harvey, Negative impact of rAAV2 mediated expression of SOCS3 on the regeneration of adult retinal ganglion cell axons, Mol. Cell. Neurosci. 46 (2011) 507–515, https://doi.org/10.1016/j.mcn.2010.12.003.

[32] M.A. Kanow, M.M. Giarmarco, C.S. Jankowski, K. Tsantilas, A.L. Engel, J. Du, J. D. Linton, C.C. Farnsworth, S.R. Sloat, A. Rountree, et al., Biochemical adaptations of the retina and retinal pigment epithelium support a metabolic ecosystem in the vertebrate eye, eLife 6 (2017) e28899, https://doi.org/10.7554/eLife.28899.

[33] A.K. Patel, S. Syeda, A.S. Hackam, Signal transducer and activator of transcription 3 (STAT3) signaling in retinal pigment epithelium cells, JAK-STAT 2 (2013) e25434, https://doi.org/10.4161/jkst.25434.

[34] J. Burke, Epithelial phenotype and the RPE: is the answer blowing in the Wnt? Prog. Retin. Eye Res. 27 (2008) 579–595, https://doi.org/10.1016/j.preteyeres.2008.08.002.

[35] M.M. LaVail, K. Unoki, D. Yasumura, M.T. Matthes, G.D. Yancopoulos, R. H. Steinberg, Multiple growth factors, cytokines, and neurotrophins rescue photoreceptors from the damaging effects of constant light, Proc. Natl. Acad. Sci. USA 89 (1992) 11249–11253, https://doi.org/10.1073/pnas.89.23.11249.

[36] Y. Xu, L. Ma, Y. Wang, C. Shi, Engineering strategies of biomaterial-assisted exosomes for skin wound repair: latest advances and challenges, Chin. Chem. Lett. 36 (2025) 109766, https://doi.org/10.1016/j.cclet.2024.109766.

[37] J. Liu, X. Wang, Y. Wu, L. Yuan, X. Zhang, X. Wu, M. Liu, Fabrication of hairpin DNA-functionalized polydopamine-coated gold nanoparticles as a theranostic nanoplatform for effective delivery of daunorubicin: binding affinity, drug release and cytotoxicity study, J. Drug Delivery Sci. Technol. 116 (2026) 107982, https://doi.org/10.1016/j.jddst.2026.107982.

[38] L. Macchioni, D. Chiasserini, L. Mezzasoma, M. Davidescu, P.L. Orvietani, K. Fettucciari, L. Salviati, B. Cellini, I. Bellezza, Crosstalk between long-term sublethal oxidative stress and detrimental inflammation as potential drivers for age-related retinal degeneration, Antioxidants 10 (2020) 25, https://doi.org/10.3390/antiox10010025.

[39] Y. Markitantova, V. Simirskii, Endogenous and exogenous regulation of redox homeostasis in retinal pigment epithelium cells: an updated antioxidant perspective, Int. J. Mol. Sci. 24 (2023) 10776, https://doi.org/10.3390/ijms241310776.

[40] S. Chen, N.A. Popp, C.-C. Chan, Animal models of age-related macular degeneration and their translatability into the clinic, Expert Rev. Ophthalmol. 9 (2014) 285–295, https://doi.org/10.1586/17469899.2014.939171.

[41] X.-Y. Zhang, T.K. Ng, M.E. Brelén, D. Wu, J.X. Wang, K.P. Chan, J.S.Y. Yung, D. Cao, Y. Wang, S. Zhang, et al., Continuous exposure to non-lethal doses of sodium iodate induces retinal pigment epithelial cell dysfunction, Sci. Rep. 6 (2016) 37279, https://doi.org/10.1038/srep37279.

[42] M.R. Biswal, H.M. Prentice, C.K. Dorey, J.C. Blanks, A hypoxia-responsive glial cell-specific gene therapy vector for targeting retinal neovascularization, Invest. Ophthalmol. Vis. Sci. 55 (2014) 8044–8053, https://doi.org/10.1167/iovs.14-13932.

[43] K. She, Y. Liu, Q. Zhao, X. Jin, Y. Yang, J. Su, R. Li, L. Song, J. Xiao, S. Yao, et al., Dual-AAV split prime editor corrects the mutation and phenotype in mice with inherited retinal degeneration, Signal Transduct. Target. Ther. 8 (2023) 57, https://doi.org/10.1038/s41392-022-01234-1.